Department of Construction Sciences
Solid Mechanics

ISRN LUTFD2/TFHF-21/5245-SE(1-49)

Topology optimization: perimeter restriction using total variation

Master's Dissertation by

Jonas Fredriksson

Supervisors:
Prof. Mathias Wallin, Div. of Solid Mechanics, Lund University
Prof. Martin Berggren, Dep. of Computing Science, Umeå University
Prof. Eddie Wadbro, Dep. of Mathematics and Computer Science, Karlstad University
Postdoctoral fellow Linus Hägg, Dep. of Computing Science, Umeå University

Examiner:
Assoc. Prof. Håkan Hallberg, Div. of Solid Mechanics, Lund University

For information, address:
Division of Solid Mechanics, Lund University, Box 118, SE-221 00 Lund, Sweden
Webpage: www.solid.lth.se

Abstract

Topology optimization is a method used to find optimal material distributions, within a specified domain, with respect to some performance measure. To avoid various artifacts to appear in the suggested design, the solution space is typically restricted, where some restriction methods allow different length scales to be controlled in the design. The suggested material distribution may result in complex designs that are difficult and costly to manufacture. By controlling the perimeter of the design, solutions with limited complexity can be found.

In this thesis, two different methods of controlling the perimeter of the solution in topology optimization are investigated. First, a method is presented where a constraint on the total variation is added to the optimization problem. The method is evaluated by solving a 2-dimensional heat flow topology optimization problem, where two different penalization strategies are used. With the total variation constraint method, the perimeter cannot be fully controlled. However, some useful applications in engineering might still be found. For comparison, the topology optimization problem is also solved using a PDE-filter, which is modified for computational efficiency. Finally, a filter with total variation regularization is presented, without being successfully implemented.

Acknowledgements

This master thesis is submitted for a Master's Degree in Mechanical Engineering at the Division of Solid Mechanics, Lund University, and has been written in collaboration with the Department of Computing Science, Umeå University.

First of all I would like to thank my supervisors Mathias, Martin, Eddie and Linus, who have all contributed to this thesis. Without their support, guidance and encouragement this thesis would not exist. I am also thankful for being given the opportunity to write this thesis at Umeå University.

I would also like to thank Angelina for supporting me, especially during the more stressful times.

Finally, I would like to thank my family and all my friends for their support during my education.

Notations

∇ = Nabla operator
Δ = Laplacian
$\delta_{i.j}$ = Kronecker delta
FEM = finite element method
MMA = Method of Moving Asymptotes
PDE = partial differential equation
SIMP = Solid Isotropic Material with Penalization
TV = total variation
M_x = number of elements in the x-direction
M_y = number of elements in the y-direction
$M_e = M_x \times M_y$ = total number of elements
M_n = number of nodes

Contents

1 Introduction

Topology optimization is an engineering tool where a computer program is used to provide solutions to design problems. The question is where material should be placed within a specified design domain, as illustrated in figure 1a, to achieve the best possible performance. The optimization problem typically consist of an objective, with one or several constraints. A common objective is to maximize the stiffness of a structure with a typical constraint on the volume, or area, of the design. However, many other problems may be solved including heat flow and stress optimization. Unwanted micro-structures such as checker-boarding may appear in the solution, as seen in figure 1b. To achieve useful results, methods to avoid these unwanted solutions are needed, some of which allows the control of various length scales in the design.

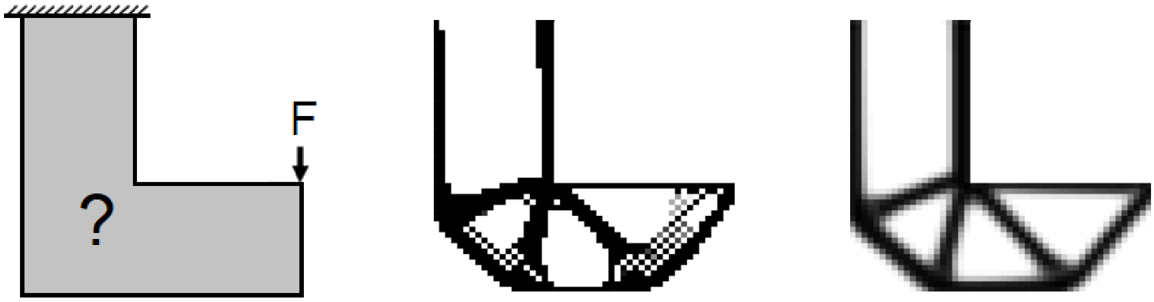

(a) (b) (c)

Figure 1: a) 2-d topology optimization problem. b) Design obtained from stiffness optimization with a volume constraint without filter. c) Design obtained from stiffness optimization with a volume constraint and a density filter.

A common method is to apply a density filter [4] that filters away any structure smaller than a specified size, which was used to achieve the design in figure 1c. The suggested designs could be highly complex demanding the use of expensive manufacturing methods. It can therefore be of interest to find designs with limited complexity, which can be done by controlling the perimeter of the solution, that is, the length of the boundary segments in a 2-dimensional design.

The aim of this thesis is to implement and evaluate a method to control the perimeter of the design in a 2-dimensional heat flow problem using the so-called total variation, defined in section 4.1.

The thesis begins with a brief description of the topology optimization method used throughout the work and a description of common restriction methods. The optimization problem investigated throughout this thesis is then introduced, followed by the different restriction methods that have been implemented, starting with total variation constraint. For comparison, a PDE-filter with a modification for improved computational efficiency is implemented and finally a filter with total variation regularization is presented. This is followed by the results, discussion and conclusions for the three investigated restriction methods.

2 Toplogy optimization

2.1 Density-based topology optimization

To be able to solve the topology optimization problem, the state problem, the equation that describes the physical behaviour of the system, must be evaluated with respect to the material distribution. Therefore, a method to distinguish between material and void in the design domain must be introduced. In density-based topology optimization [1] the material distribution is described by an artificial density $\rho = \rho(x, y)$, where the term artificial is used since the density is not coupled to the weight of the design but to the amount of material placed in the design domain. Areas where material should be placed are represented by $\rho = 1$, while areas where $\rho = 0$ should be left empty. In this thesis, the state problem is solved by the finite element method, where the density is coupled to the finite element equation via the stiffness matrix. To allow the use of gradient based solution algorithms, ρ is allowed to vary continuously on $0 < \rho < 1$. However, the intermediate densities has no physical interpretation and a discrete solution where ρ is binary is therefore sought. Since the results are often displayed as grey-scale images with $\rho = 1$ being black and $\rho = 0$ being white, a binary solution is often referred to as a crisp black and white solution.

A way of measuring how far the solution is from being binary is the "measure of non-discreteness" [21]

$$M_{nd} = \frac{4\sum_{i=1}^{M_e} \rho_i(1-\rho_i)}{M_e}, \tag{1}$$

where M_e is the number of elements. $M_{nd} = 0$ when ρ is binary and takes the maximal value 1 when the density of all elements is 0.5.

2.2 Penalization

To achieve a crisp black and white solution, intermediate densities must be penalized in the problem formulation. Several approaches to penalize intermediate densities has been proposed in the literature. A straightforward approach is to add a penalty term to the objective function on the form $\beta f(\rho)$ [9], where β is a constant that allows the amount of penalization to be controlled and $f(\rho)$ is chosen depending on the design problem and whether the objective function is minimized or maximized.

SIMP (Solid Isotropic Material with Penalization) introduced by Bendsøe and Kikuchi [1] is another penalization method where the stiffness matrix is calculated using ρ^q instead of ρ , with the SIMP-parameter $1 \leq q$. This lowers the stiffness of elements with intermediate densities, thus reducing their relative performance. $q = 3$ or $q = 4$ are common values for the SIMP-parameter for mechanical compliance problems, but for heat flow problems a larger SIMP-parameter is often needed to achieve a crisp black and white solution [8].

With penalization, a nearly crisp black and white solution can be achieved, but the solution may be mesh-dependent with micro-structures in the design such as checker-boarding, as illustrated in figure 1b. Checker-boarding patterns were previously thought to be an optimal micro-structure design, but it has been proven by Diaz and Sigmund [5] and Jog and Haber [2] that the stiffness of the checker-boarding patterns are overestimated due to numerical limitations of low order finite element methods. Since the aim is to find designs that can be realized, mesh-dependent micro structures are unwanted in the design. Two ways of avoiding these solutions are to introduce a filter or to impose a bound on the perimeter of the design.

2.3 Filtering methods

The so called sensitivity filtering was introduced by Sigmund [17] [22]. The filter consists of a local average of the objective function derivatives in the form

$$\frac{\widehat{\partial f}}{\partial \rho_k} = (\rho_k)^{-1} \frac{1}{\sum_{i=1}^{M_e} w_j} \sum_{i=1}^{M_e} w_j \rho_i \frac{\partial f}{\partial \rho_i}, \tag{2}$$

where the filtered sensitivities (derivatives) are $\frac{\widehat{\partial f}}{\partial \rho_k}$ and the true sensitives are $\frac{\partial f}{\partial \rho_i}$.

In the density filter, suggested by Bruns and Tortorelli [4], each element density is a weighted mean value of all element densities within a specified radius r. The density filter thereby introduces a characteristic length scale, a minimum radius of any member in the design which can be coupled to a manufacturing constraint such as a minimum end mill radius. The filtered density $\tilde{\rho}$ of each element is described on the form

$$\tilde{\rho}_i(\boldsymbol{\rho}) = \sum_{j}^{M_e} \frac{w_j(x_i,\ x_j,\ y_i,\ y_j,\ r)\rho_j}{w}, \tag{3}$$

where $\sum_j^{M_e}$ is the sum over all elements, (x_k, y_k) are the coordinates of element k, w_j is the weight function and $w = \sum_j^{M_e} w_j$. Bruns and Tortorelli [4] suggest a weight function that is decreasing with the square of the distance from the element center, although any meaningful weight function may be used.

The PDE-filter, first proposed by Lazarov and Sigmund [14] and later modified by Wallin et al. [3] to mitigate issues with designs sticking to the design domain boundaries, relies on minimizing a potential function where there is a competition between the gradients of the filtered variables and the differences between the filtered and the unfiltered variable. Minimization of the potential function results in a partial differential equation (PDE) that can be solved using the finite element method on the same mesh as the state problem. An implementation of the PDE-filter is done in chapter-5.

Other restriction methods found in literature are level set methods [6] where use is made of the local scattering function (LSF), phase-field filtering [16] where the length scale penalization is include in the objective and perimeter control [9], which is the main subject in this thesis.

2.4 Perimeter control

Several approaches to perimeter control has been suggested in the literature. In the "perimeter method" [9] the perimeter is controlled by including a logarithmic function of the perimeter in the objective function on the form $\beta f(P)$, where the constant β is varied through the iterations. Beckers [15] implemented a method with a perimeter constraint on a binary design variable, with satisfying results when applied to a mechanical compliance problem. Duysinx [19] and Borrvall [23] implemented perimeter control on a mechanical compliance problem. In these works, the perimeter is estimated using numerical approximations of the total variation of ρ. Since the total variation is an accurate measure of the perimeter when ρ is binary, the demand of a binary solution is emphasized.

2.5 Solving the optimization problem

Iterative algorithms are used to solve the optimization problem. Gradient-based optimization algorithms are commonly used in topology optimization [19] with Convex Linear Approximation (CONLIN) and the Method of Moving Asymptotes (MMA) [13] being two of the most frequently used methods. The latter is chosen for the implementations in this thesis since it has, according to Duysinx [19], been proven to be more numerically stable when applied to difficult problems. Other optimization algorithms such as meta-heuristics and genetic algorithms exist but are typically not applicable for this topology optimization problem due to the large number of state evaluations they need.

Since the MMA is gradient based, derivatives with respect to the design variable ρ of the objective function as well as the constraints, need to be computed at each iteration. Topology optimization problems are typically non-convex, thus multiple local optima may exist, and the solution algorithm may converge to one of these local optima, that may be highly sub-optimal. It should therefore be noted that there is no guarantee that the problem converges to an optimal solution. Also, in topology optimization, there may not be one optimal solution but finitely many. However, in engineering it is most often satisfactory to find a solution that improves performance.

3 Optimization problem

3.1 ”Heat compliance” minimization problem

The ”heat compliance” minimization problem investigated in this thesis is a standard model problem in density based topology optimization [8]. The goal is to optimize the heat dissipation by minimizing the ”heat compliance” of a 2-dimensional homogeneous isotropic plate that is subject to uniform heating with a constraint on the area of the design. The design is represented by a material distribution, given by an artificial dimensionless density $\rho = \rho(x, y)$ that takes the values $0 \leq \rho \leq 1$. The area of the design is defined as $A = \int_\Omega \rho \, dA$ and is the physical area of the design when ρ is binary. The temperature of the plate is determined using the finite element method.

The design domain Ω, illustrated in figure 2, is a square with side length $L = 1$ m and with boundary Γ consisting of the two parts Γ_N and Γ_D. The boundary is perfectly insulated at Γ_N, and at Γ_D the temperature is fixed at 0. The heat conductivity of the isotropic material is defined by $\alpha = 1$ W/(m $\cdot$ K) and the design domain is subject to an evenly distributed heat load $Q = 4$ W/m^2 that is independent of ρ.

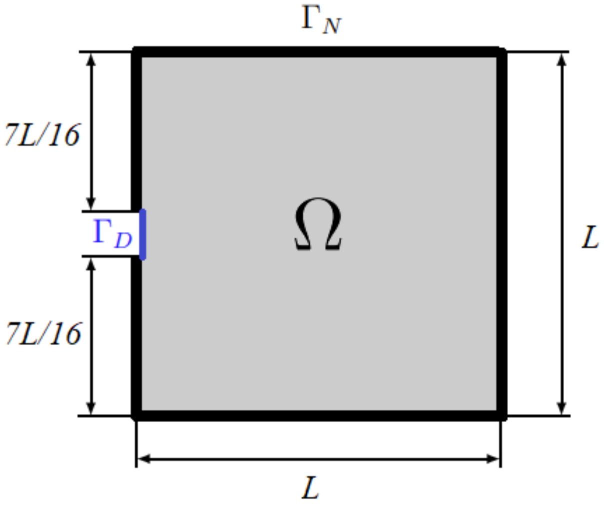

Figure 2: Geometry and design domain for the minimum heat compliance problem.

3.2 Discrete form of the ”heat compliance” minimization problem

The design domain is discretized into a uniform mesh with $M_e = M_x \times M_y$ 4-node elements and the density field is assumed to be element-wise constant represented by the density vector $\boldsymbol{\rho}$. A summary of the finite element formulation can be found in box 1, while the derivation of the expressions can be found in Appendix B. 4-node bi-linear square elements are chosen for computational efficiency, instead of the more commonly used isoparametric elements [10]. The element shape functions are

$$\begin{aligned} N_1^e(x,y) &= \frac{1}{h^2}(x-x_2)(y-y_4), \\ N_2^e(x,y) &= -\frac{1}{h^2}(x-x_1)(y-y_3), \\ N_3^e(x,y) &= \frac{1}{h^2}(x-x_4)(y-y_2), \\ N_4^e(x,y) &= -\frac{1}{h^2}(x-x_3)(y-y_1), \end{aligned} \tag{4}$$

where h is the side length of the element and the elements are aligned with the coordinate axes, as illustrated in figure 3.

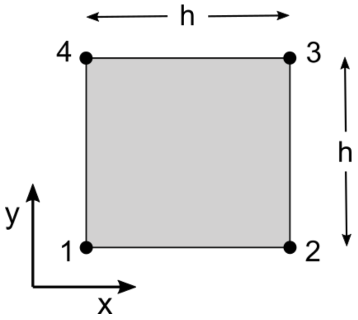

Figure 3: 4-node square element with side length h.

$$\boldsymbol{K}(\rho)\boldsymbol{u} = \boldsymbol{f}, \tag{5}$$

with
$\boldsymbol{K}(\rho) = \int_\Omega P(\rho)\boldsymbol{B^T D B}\; dA$ stiffness matrix ,
$\boldsymbol{f} = \boldsymbol{f_l} = \int_\Omega \boldsymbol{N^T} Q\; dA$ load vector ,
$\boldsymbol{u}$ node temperature vector containing the unknown node temperatures,
$\boldsymbol{D} = \alpha \boldsymbol{I}$ constitutive matrix,
$\boldsymbol{N} = [\boldsymbol{N^1 N^2} ... \boldsymbol{N^n}]$ global element shape function matrix,
$\boldsymbol{N^e} = [N_1^e\ N_2^e\ N_3^e\ N_4^e]^T$. contains the element shape functions for element e,
$\boldsymbol{B = \nabla N}$,

Box 1: Finite element formulation.

The global stiffness matrix $\boldsymbol{K}(\rho)$ is computed element-wise and is then assembled using the FEM assembly routine denoted $\sum\!\!\!\!\sum$, i.e.

$$\boldsymbol{K} = \sum\!\!\!\!\sum \boldsymbol{K}_i^e(\rho), \tag{6}$$

where

$$\boldsymbol{K_i^e}(\rho) = \int_{\Omega_i^e} P(\rho)\boldsymbol{B^{eT} D B^e}\; dA \tag{7}$$

and $P(\rho)$ is the penalized density, to be specified below. If ρ is element-wise constant and represented by the density vector $\boldsymbol{\rho} = [\rho_1, \rho_2 \ ... \ \rho_{M_e}]^T$, with M_e being the number of elements,

$$\boldsymbol{K_i^e}(\rho_i) = P(\rho_i)\boldsymbol{K_{0,i}^e} = P(\rho_i)\int_{\Omega_i^e} \boldsymbol{B^{eT} D B^e} \ dA \tag{8}$$

where the penalised density scales the corresponding element stiffness matrix. The "heat compliance" is calculated as $\boldsymbol{f^T u}$ and is proportional to the average temperature of the design domain, Ω, since the heat load is evenly distributed. The discrete optimization problem may be written as

$$\begin{aligned} \min_{\boldsymbol{\rho},\boldsymbol{u}} \quad & g_0 = \boldsymbol{f^T u} \\ \text{subject to:} \quad & \begin{cases} A(\boldsymbol{\rho}) \leq \omega A_0 \\ \boldsymbol{K(\rho)u = f}, \end{cases} \end{aligned} \tag{9}$$

where $A(\boldsymbol{\rho}) = \mathbb{1}^T \boldsymbol{\rho} h^2$, $\mathbb{1}$ is a column vector with the same length as $\boldsymbol{\rho}$ with the values 1 at each index, A_0 is the total area of the design domain, $0 < \omega < 1$ is a constant and $\boldsymbol{K(\rho)u = f}$ is the finite element equation (5).

3.3 Penalization

With the standard SIMP-scheme, the penalized density is $P(\rho_i) = \rho_i^q$. Since the heat load Q is distributed evenly over the design domain, a minimum value $\underline{p}$ for the scaling of the stiffness matrix must be introduced to allow heat to be dissipated from the void areas and to avoid a singular stiffness matrix. A relatively large value of $\underline{p}$, compared to mechanical compliance problems where the load is typically not evenly distributed, is needed. Otherwise the solution algorithm tends to increase the density in the void areas, resulting in a solution where the performance is not only dependent on the material distribution, but also on the contrast between the void areas and the areas with material.

Modified SIMP-scheme

The modified SIMP-scheme, used by Hägg and Wadbro [7], with the penalization function

$$P(\rho_i) = \underline{p} + (1 - \underline{p})\rho_i^q \tag{10}$$

is used, where q is the SIMP-parameter and $\underline{p} = 10^{-3}$ defines the minimum value for the penalized density. To achieve a discrete solution, a continuation strategy [7] is used where the problem is solved for $q = 1, 2, 3...10$.

Combined penalization

In the combined penalization method, the modified SIMP-scheme, with a constant SIMP-parameter $q = 3$, is used together with an added term to the goal function

$$c_1(n,h)\boldsymbol{\rho}^T(\mathbb{1} - \boldsymbol{\rho}). \tag{11}$$

In analogy with the continuation method used for the modified SIMP-scheme, the parameter $c_1(n,h) = kh(2.2^n)$ is increased, where $k = 0.125$, h is the element side length and the problem is solved for $n = 1, 2...14$.

3.4 Solution method

In this thesis all optimization programs are implemented in Matlab using a MMA-solver implemented by K. Svanberg, which is available under a ”free license” and can be downloaded from the authors website [12]. A full description of the MMA-code can be found in [11].

3.5 Sensitivity analysis

The objective in (9) reads $g_0 = \boldsymbol{f^T u}$, where $\boldsymbol{f}$ is constant. Differentiation of g_0 with respect to ρ_i yields

$$\frac{\partial g_0}{\partial \rho_i} = \frac{\partial}{\partial \rho_i}(\boldsymbol{f}^T\boldsymbol{u}) = \boldsymbol{f}^T\frac{\partial \boldsymbol{u}}{\partial \rho_i} = \boldsymbol{u}^T\boldsymbol{K}\frac{\partial \boldsymbol{u}}{\partial \rho_i}, \tag{12}$$

where equation (5) was used in the last step. Since $\frac{\partial \boldsymbol{f}}{\partial \rho_j} = 0$ and $\boldsymbol{f} = \boldsymbol{K}\boldsymbol{u}$, by eq. (5),

$$0 = \frac{\partial \boldsymbol{f}}{\partial \rho_i} = \frac{\partial \boldsymbol{K}}{\partial \rho_i}\boldsymbol{u} + \boldsymbol{K}\frac{\partial \boldsymbol{u}}{\partial \rho_i} \;\Rightarrow\; \frac{\partial \boldsymbol{u}}{\partial \rho_i} = -\boldsymbol{K}^{-1}\frac{\partial \boldsymbol{K}}{\partial \rho_i}\boldsymbol{u} \tag{13}$$

which together with (12) gives

$$\frac{\partial g_0}{\partial \rho_i} = -\boldsymbol{u}^T\frac{\partial \boldsymbol{K}}{\partial \rho_i}\boldsymbol{u}. \tag{14}$$

When the density is element-wise constant, expressions (6), (8) and (14) can be used to conclude that

$$\frac{\partial g_0}{\partial \rho_i} = -\boldsymbol{u}_i^{eT}\frac{\partial \boldsymbol{K}_i^e}{\partial \rho_i}\boldsymbol{u}_i^e = -\frac{\partial P(\rho_i)}{\partial \rho_i}\boldsymbol{u}_i^{eT}\boldsymbol{K_{0,i}^e}\boldsymbol{u}_i^e, \tag{15}$$

where $\boldsymbol{u}_i^e$ is a vector containing the node temperatures for element i and $\boldsymbol{K}_i^e$ is the element stiffness matrix for element i.

The sensitivity of the area constraint is trivially calculated as

$$\frac{\partial A(\boldsymbol{\rho})}{\partial \rho_i} = h^2, \tag{16}$$

and is the same for all index i since all elements are equally sized.

4 Total variation constraint

4.1 Optimization problem

To impose a bound on the perimeter of the design, the optimization problem (9) is modified by including the total variation as a constraint. The optimization problem may then be written as

$$\begin{aligned} &\min_{\boldsymbol{\rho},\boldsymbol{u}} \quad g_0 = \boldsymbol{f}^{\boldsymbol{T}}\boldsymbol{u}, \\ &\text{subject to:} \begin{cases} TV(\boldsymbol{\rho}) \leq \tau \\ A(\boldsymbol{\rho}) \leq \omega V_0 \\ \boldsymbol{K}(\boldsymbol{\rho})\boldsymbol{u} = \boldsymbol{f}, \end{cases} \end{aligned} \tag{17}$$

where $TV(\boldsymbol{\rho})$ is an approximation of the total variation of the elementwise constant density field, represented by the density vector $\boldsymbol{\rho}$, and τ is the upper limit of the perimeter. For a smooth density field the total variation is defined as

$$TV = \int_{\Omega} |\nabla\rho| dA = \int_{\Omega} \sqrt{\nabla\rho\cdot\nabla\rho}\; dA. \tag{18}$$

However, element-wise constant fields are in general not smooth. A definition of the total variation of a non-smooth field exists and can be found in [23], but for practical reasons, a numerical approximation introduced by Borrvall [23] is used here.

4.2 Numerical approximation of Total Variation

For an element-wise constant density distribution, it is not obvious how $|\nabla\rho|$ should be interpreted and computed. A method where the gradients are estimated using finite differences of element densities is suggested by Borrvall [23], where, due to the discretization of the density distribution as element-wise constant, a fully isotropic approximation of the total variation is not possible to obtain. Borrvall suggests several expressions where differences are evaluated in different directions. TV_4 is chosen here since it is least anisotropic of the alternatives,

$$\begin{aligned} TV_4(\boldsymbol{\rho}) = (\sqrt{2}-1)h &\left(\sum_{i=1}^{M_x-1}\sum_{j=1}^{M_y}\delta^x_{i,j} + \sum_{i=1}^{M_x}\sum_{j=1}^{M_y-1}\delta^y_{i,j})\right) \\ +\frac{\sqrt{2}-1}{\sqrt{2}}h &\left(\sum_{i=2}^{M_x}\sum_{j=1}^{M_y-1}\delta^{xy}_{i,j} + \sum_{i=1}^{M_x-1}\sum_{j=1}^{M_y-1}\delta^{yx}_{i,j}\right), \end{aligned} \tag{19}$$

where M_x, M_y is the number of elements in the x- and y-direction respectively. The finite differences $\delta^x_{i,j}, \delta^y_{i,j}, \delta^{xy}_{i,j}, \delta^{yx}_{i,j}$ used in (19) are defined as

$$\begin{aligned}\delta^x_{i,j} &= |\rho_{i+1,j} - \rho_{i,j}|,\\ \delta^y_{i,j} &= |\rho_{i,j+1} - \rho_{i,j}|,\\ \delta^{xy}_{i,j} &= |\rho_{i-1,j+1} - \rho_{i,j}|,\\ \delta^{yx}_{i,j} &= |\rho_{i+1,j+1} - \rho_{i,j}|,\end{aligned} \tag{20}$$

where $\rho_{i+M_x(j-1)} = \rho_{i,j}$. The finite differences in (20) are illustrated in figure 4b. To include the elements on the edges of the design domain when the perimeter is estimated, TV_4 must be computed in an extended domain Ω^*. The extended domain, illustrated in figure 4a, consists of the design domain Ω in grey, with a surrounding layer of elements with zero density in white.

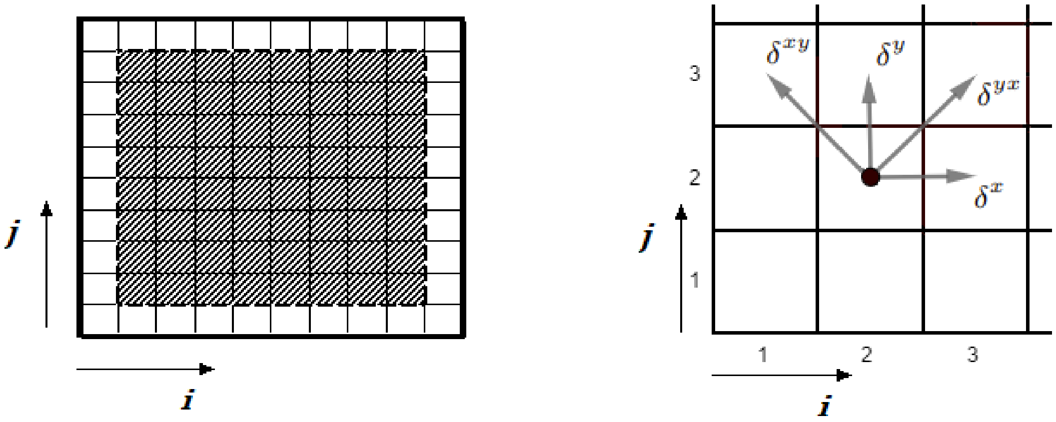

(a)

(b)

Figure 4: a) The design domain Ω (grey), discretized into $M_x \times M_y = 8 \times 8$ elements, and the extended domain Ω^* (white + grey). b) Finite differences at index $(i,j) = (2,2)$ in the four directions.

As seen in figure 4a, the extended domain has 2 more elements in the x and y-direction, respectively. Subsequently, if the same indexing (i,j) is used, starting at the bottom left corner of Ω and Ω^* respectively, $\rho_{i,j} = \rho^*_{i+1,j+1}$, where $\boldsymbol{\rho}^*$ is the extended density vector containing the element densities in the extended domain Ω^*. The total variation is calculated in the extended domain as

$$\begin{aligned} TV_4(\boldsymbol{\rho}^*) = TV_4^x(\boldsymbol{\rho}^*) + TV_4^y(\boldsymbol{\rho}^*) + TV_4^{xy}(\boldsymbol{\rho}^*) + TV_4^{yx}(\boldsymbol{\rho}^*) = \\ (\sqrt{2}-1)h\left(\sum_{i=1}^{M_x+1}\sum_{j=2}^{M_y+1}\delta^x_{i,j} + \sum_{i=2}^{M_x+1}\sum_{j=1}^{M_y+1}\delta^y_{i,j})\right) \\ +\frac{\sqrt{2}-1}{\sqrt{2}}h\left(\sum_{i=2}^{M_x+2}\sum_{j=1}^{M_y+1}\delta^{xy}_{i,j} + \sum_{i=1}^{M_x+1}\sum_{j=1}^{M_y+1}\delta^{yx}_{i,j}\right). \end{aligned} \tag{21}$$

Since $|x|$, in expression (20), is not differentiable at $x = 0$, and the solution algorithm (MMA) requires the sensitivities to be calculated, a smooth approximation of the absolute value function is needed. The first smooth approximation that is considered is

$$|x| \approx f_1(x) = (x^2 + \epsilon^2)^{1/2} - \epsilon, \tag{22}$$

where $\epsilon > 0$, which was used by Beckers [15]. The approximation (22) satisfies $f_1(0; \epsilon) = 0$ and $f_1(x; \epsilon) \longrightarrow |x|$ when $\epsilon \longrightarrow 0$. The second smooth approximation that is considered is

$$|x| \approx f_2(x) = [(1 + 2\epsilon)x^2 + \epsilon^2]^{1/2} - \epsilon, \tag{23}$$

used by Haber et al. [9]. The advantage of approximation (23) compared to approximation (22) is that not only $f_2(0; \epsilon) = 0$ and $f_2(x; \epsilon) \longrightarrow |x|$ when $\epsilon \longrightarrow 0$ hold, but also $f_2(1; \epsilon) = 1$ holds, meaning that the approximation is exact when ρ is binary.

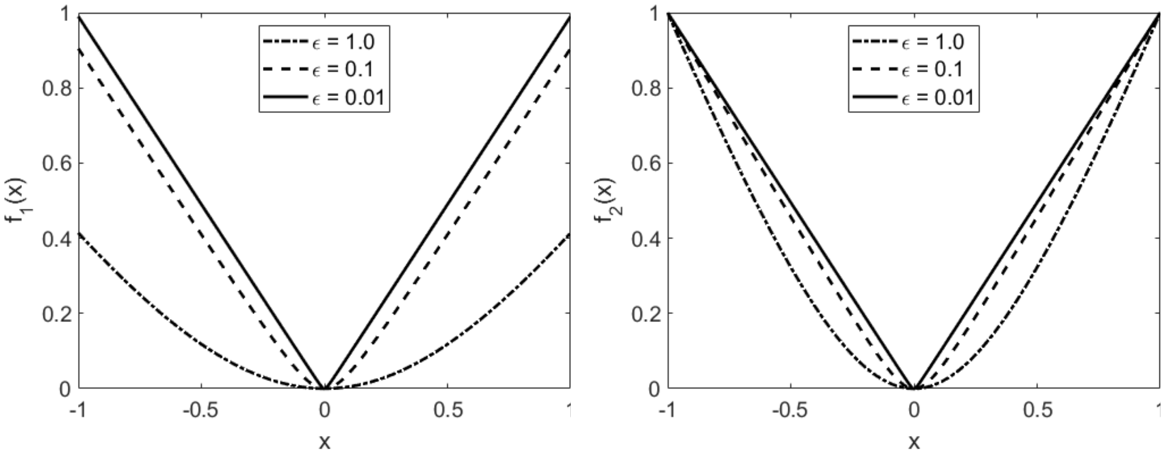

(a)

(b)

Figure 5: Comparison of smooth approximations with different values of ϵ. a) f_1 b) f_2

As can be seen in figure 5, the smooth approximations in (22) and (23) are underestimating the absolute function at a large part of the interval which leads to an underestimation of the total variation. This is illustrated by computing the one-dimensional total variation of a transition from $\rho = 1$ to $\rho = 0$ over a set of elements where the finite differences $\delta_i = \rho_i - \rho_{i+1} = \delta_\rho$ are equally sized as in figure 6.

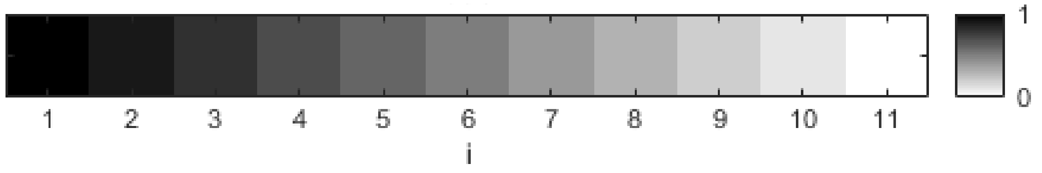

Figure 6: Transition from $\rho = 1$ to $\rho = 0$ over 11 elements, with 10 equally sized finite differences $\delta_\rho = \rho_i - \rho_{i+1} = 0.1$.

The one-dimensional total variation is calculated as

$$TV_1 = \sum_{i=1}^{1/\delta_\rho} f_n(\delta_\rho) = \frac{1}{\delta_\rho} f_n(\delta_\rho), \tag{24}$$

where $\delta_\rho = \rho_i - \rho_{i+1}$ is the step size and $1/\delta_\rho$ is the number of finite differences used to discretize the transition from $\rho = 1$ to $\rho = 0$. If the absolute function is used $TV_1 = 1$, for $\delta_\rho > 0$. Equation (24) is illustrated in figure 7 where f_1 is used in figure 7a and f_2 in 7b. Since equation (24) is a growing function on $0 < \delta_\rho < 1$ for any $0 < \epsilon < 1$, while the "true" total variation is 1 for any $\delta_\rho > 0$. It can be concluded that the underestimation of the total variation increases as the finite difference size δ_ρ decreases, $TV_1 \longrightarrow 0$ as $\delta_\rho \longrightarrow 0$, which holds for both f_1 and f_2.

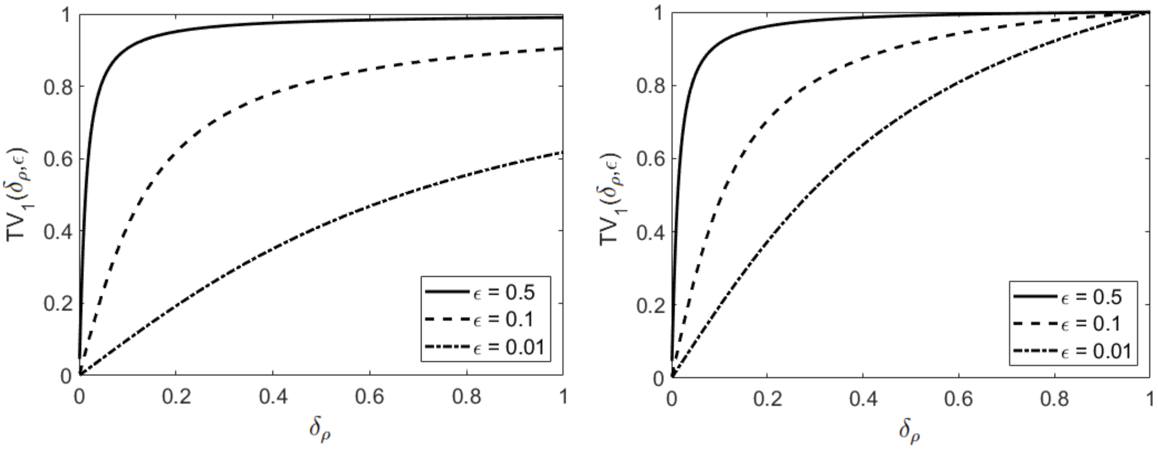

(a) (b)

Figure 7: Total variation dependence of step size δ_ρ for a transition from $\rho_i = 1$ to $\rho_{i+n} = 0$ for three different values of ϵ. a) f_1 b) f_2

Accuracy and anisotropic properties

Due to the inherent anisotropy of the finite element discretization, TV_4 is an anisotropic measure of the perimeter that is only accurate for a design with crisp edges that are parallel to the coordinate axis or at 45° angle to the coordinate axis. For other angles, the perimeter is overestimated with a maximum of 8 percent at 22.5° angle, according to Borrvall [23].

To evaluate the accuracy of TV_4 for designs with blurred edges, the perimeter is calculated on a set of black discs with blurred edges, that are discretized into 256×256 elements with element-wise constant density, and compared to the "area". More precisely, a normalized ratio between TV_4 and the "area" of the discs is computed as

$$Q(\boldsymbol{\rho}) = TV_4(\boldsymbol{\rho})/(2\sqrt{\pi A(\boldsymbol{\rho})}), \tag{25}$$

where $Q = 1$ is the ratio if the measurements of the perimeter and the "area" are exact. The discs are defined by an inner radius (R_i) and an outer radius (R_o)

$$\rho_i = \begin{cases} 1 \quad r < R_i \\ g_n(r) \quad R_i \le r \le R_o \\ 0 \quad r > R_o \ , \end{cases} \tag{26}$$

where $g_n(r)$ is a decreasing function of the distance from the center of the design domain to the element center r. The following functions where used

$$\begin{aligned} g_1(r) &= \frac{\sqrt{(R_o - r)}}{\sqrt{(R_o - R_i)}}, \\ g_2(r) &= \frac{R_o - r}{R_o - R_i}, \\ g_3(r) &= \frac{(R_o - r)^2}{(R_o - R_i)^2}. \end{aligned} \tag{27}$$

To evaluate TV_4 and not the smooth approximations f_n, TV_4 is calculated using the absolute values instead of a smooth approximation.

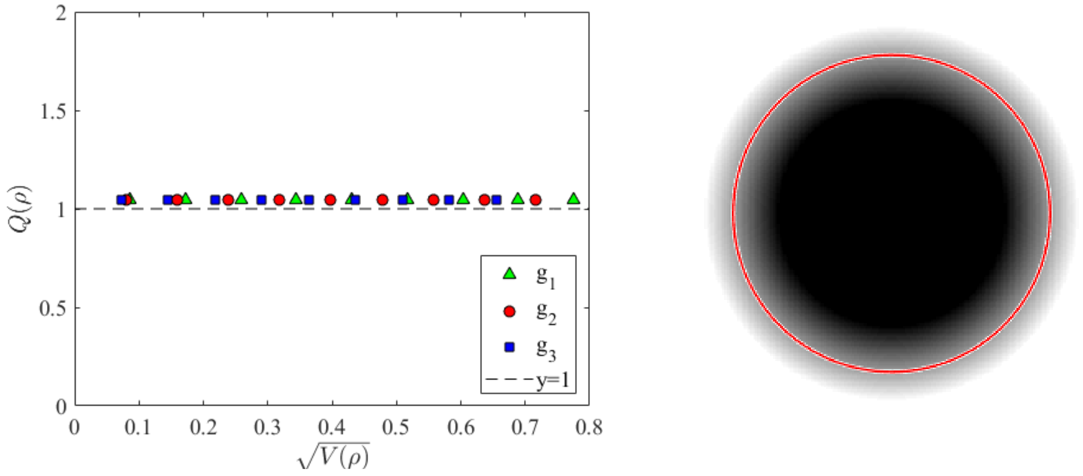

(a)

(b)

Figure 8: Results from the geometric analysis. a) Normalized ratio (25) between TV_4 and $A(\boldsymbol{\rho})$. b) Graphic illustration of the calculated perimeter $TV_4 = 1.767$ (red) of a circle with blurred edges ($g_2(R_i = 1.257; R_o = 2.094)$).

4.3 Sensitivty analysis

To compute derivatives of TV_4 with respect to the density, we consider (21) and conclude that

$$\frac{\partial TV_4}{\partial \rho^*_{i,j}} = \frac{\partial TV_4^x}{\partial \rho^*_{i,j}} + \frac{\partial TV_4^y}{\partial \rho^*_{i,j}} + \frac{\partial TV_4^{xy}}{\partial \rho^*_{i,j}} + \frac{\partial TV_4^{yx}}{\partial \rho^*_{i,j}}. \tag{28}$$

We focus the analysis on the first term, since the same approach may then be used for the remaining terms in (28). Equation (21) yields

$$\frac{\partial TV_4^x}{\partial \rho^*_{i,j}} = (\sqrt{2}-1)h \sum_{k=1}^{M_x+1} \sum_{l=2}^{M_y+1} \frac{\partial \delta^x_{k,l}}{\partial \rho^*_{i,j}}. \tag{29}$$

From (20) we get

$$\frac{\partial \delta^x_{k,l}}{\partial \rho^*_{i,j}} = f_n'(\rho^*_{k+1,l} - \rho^*_{k,l})(\delta_{k,i}\delta_{l,j} + \delta_{k+1,i}\delta_{l,j}), \tag{30}$$

where $\delta_{i,j}$ is the Kronecker delta with the properties that $\delta_{m,n} = 1$, if $m = n$, otherwise $\delta_{m,n} = 0$. Insertion of (30) into (29) gives

$$\begin{aligned} \frac{\partial TV_4^x}{\partial \rho^*_{i,j}} &= (\sqrt{2}-1)h(\frac{\partial \delta^x_{i,j}}{\partial \rho^*_{i,j}} + \frac{\partial \delta^x_{i-1,j}}{\partial \rho^*_{i,j}}) \\ &= (\sqrt{2}-1)(h)f_n'(\rho^*_{k+1,l} - \rho^*_{k,l})(\delta_{k,i}\delta_{l,j} + \delta_{k+1,i}\delta_{l,j}). \end{aligned} \tag{31}$$

Treating the remaining terms in expression (28) analogously, we obtain

$$\frac{\partial TV_4^y}{\partial \rho^*_{i,j}} = (\sqrt{2}-1)(h)f_n'(\rho^*_{k,l+1} - \rho_{k,l})(\delta_{k,i}\delta_{l,j} + \delta_{k,i}\delta_{l+1,j}), \tag{32}$$

$$\frac{\partial TV_4^{xy}}{\partial \rho^*_{i,j}} = \frac{\sqrt{2}-1}{\sqrt{2}}(h)f_n'(\rho^*_{k-1,l+1} - \rho^*_{k,l})(\delta_{k,i}\delta_{l,j} + \delta_{k-1,i}\delta_{l+1,j}), \tag{33}$$

$$\frac{\partial TV_4^{yx}}{\partial \rho^*_{i,j}} = (\sqrt{2}-1)(h)f_n'(\rho^*_{k+1,l+1} - \rho^*_{k,l})(\delta_{k,i}\delta_{l,j} + \delta_{k+1,i}\delta_{l+1,j}). \tag{34}$$

The derivatives of the two smooth approximations defined in expression (22) and expression (23) are

$$f_1'(x) = \frac{x}{\sqrt{x^2+\epsilon^2}} = \frac{x}{f_1(x)+\epsilon}, \tag{35}$$

and

$$f_2'(x) = (1+2\epsilon)\frac{x}{\sqrt{x^2+\epsilon^2}} = (1+2\epsilon)\frac{x}{f_2(x)+\epsilon}, \tag{36}$$

respectively.

To derive the sensitivity with respect to the design variable $\boldsymbol{\rho}$, we recall that $\rho_{i,j} = \rho^*_{i+1,j+1}$, thus

$$\frac{\partial TV_4}{\partial \rho_{i,j}} = \frac{\partial TV_4}{\partial \rho^*_{i+1,j+1}}, \tag{37}$$

for $(i, j) = (1, 1)$ to $(i, j) = (M_x, M_y)$.

5 PDE-filter

In the first part of this chapter, a PDE-filter with nodal based filtered densities is implemented. In the second part, a PDE-filter is implemented, where the filtered density is element-wise constant.

5.1 Nodal based PDE-filter

The PDE-filter [14] relies on minimizing the potential functional

$$\Pi(\tilde{\rho}) = \frac{1}{2}\int_{\Omega} l_0^2 |\nabla\tilde{\rho}|^2 \; dA + \frac{1}{2}\int_{\Omega} (\rho - \tilde{\rho})^2 \; dA, \tag{38}$$

where ρ is the nominal design variable density, $\tilde{\rho}$ is the filtered density and the constant length scale parameter l_0 is related to the minimum radius of any material or void section in the solution as $r = 2\sqrt{3}l_0$ [3]. The first term is dependent on the spatial variation of $\tilde{\rho}$ and the second term is dependent on the difference between ρ and $\tilde{\rho}$. The filtered density, $\tilde{\rho}$, is obtained by minimizing the potential function with respect to $\tilde{\rho}$. The minimizer of functional (38) satisfies

$$\begin{aligned} -l_0^2\Delta\tilde{\rho} + \tilde{\rho} &= \rho \text{ in } \Omega, \\ \boldsymbol{n} \cdot \nabla\tilde{\rho} &= 0 \text{ on } \partial\Omega, \end{aligned} \tag{39}$$

which is a partial differential equation (PDE) that can be solved numerically. The PDE-filter is area conserving, which is proved by integrating the density over the entire domain,

$$A = \int_{\Omega} \rho \; dA = \int_{\Omega} l_0^2 \Delta\tilde{\rho} dA + \int_{\Omega} \tilde{\rho} \; dA. \tag{40}$$

Applying Gauss divergence theorem to the first term on the right hand side yields

$$\int_{\Omega} \rho \; dA = \int_{\partial\Omega} l_0^2 \nabla\tilde{\rho} \cdot \boldsymbol{n} \; dS + \int_{\Omega} \tilde{\rho} \; dA = \int_{\Omega} \tilde{\rho} \; dA, \tag{41}$$

where the last equality follows from $\nabla\tilde{\rho} \cdot \boldsymbol{n} = 0$ on $\partial\Omega$.

The PDE (39) is solved using the Finite Element Method on the same mesh as for the state problem. The unfiltered density ρ is element-wise constant and is represented by the vector $\boldsymbol{\rho}$ while the filtered density is interpolated using the element shape functions $\tilde{\rho} = \boldsymbol{N}\tilde{\boldsymbol{\rho}}$, where the vector $\tilde{\boldsymbol{\rho}}$ contains the nodal values of the filtered density.

In analogy with the approach used for the heat equation (see appendix B) and applying homogeneus Neumann boundary conditions on $\partial\Omega$, the discrete formulation becomes

$$l_0^2 \int_{\partial\Omega} \mathbf{B}^T\mathbf{B} \; dA \; \tilde{\boldsymbol{\rho}} + \int_{\Omega} \mathbf{N}^T\mathbf{N} \; dA \; \tilde{\boldsymbol{\rho}} = \int_{\Omega} \boldsymbol{N}^{\boldsymbol{T}} \; dA \; \boldsymbol{\rho}. \tag{42}$$

Introducing the filter operator $\hat{\boldsymbol{K}} = l_0^2 \int_\Omega \boldsymbol{B}^T \boldsymbol{B}\ dA + \int_\Omega \boldsymbol{N}^T \boldsymbol{N}\ dA$ and $\boldsymbol{T} = \int_\Omega \boldsymbol{N}^T\ dA$, expression (42) may be written as a system of linear equations on the form

$$\hat{\boldsymbol{K}} \tilde{\boldsymbol{\rho}} = \boldsymbol{T} \boldsymbol{\rho}. \tag{43}$$

Since the filtered design variable is represented as a density field that varies within the elements, expression (7) must be used when calculating the stiffness matrix for the finite element equation. To compute the element stiffness matrices Gauss quadrature with 4 Gauss points is used.

5.2 Element based PDE-filter

To construct a filter where the filtered density is element-wise constant, the nodal based PDE-filter is modified with a mapping from node values to element-wise constant values for the filtered density. The filtered element-wise constant density is represented by the vector $\hat{\boldsymbol{\rho}}$ where each element density is approximated as the average value of the four node densities

$$\hat{\rho}_i = \frac{1}{4} \sum_{j=1}^{4} \tilde{\rho}_{i,j}^e, \tag{44}$$

where i is the element index and $\tilde{\boldsymbol{\rho}}_i^e$ is a vector containing the node densities for element i. This can be expressed as a linear equation

$$\hat{\boldsymbol{\rho}} = \hat{\boldsymbol{T}} \tilde{\boldsymbol{\rho}}, \tag{45}$$

where $\hat{\boldsymbol{T}}$ is the averaging operator. The stiffness matrix in the finite element equation (5) is now evaluated with respect to $\hat{\boldsymbol{\rho}}$ using expression (8).

5.3 Sensitivity analysis

Nodal based PDE-filter

To derive the derivative of the objective function with respect to the design variable $\boldsymbol{\rho}$, we make use of the chain rule, that is,

$$\frac{\partial g_0}{\partial \boldsymbol{\rho}} = \frac{\partial g_0}{\partial \tilde{\boldsymbol{\rho}}} \frac{\partial \tilde{\boldsymbol{\rho}}}{\partial \boldsymbol{\rho}}. \tag{46}$$

The first term on the right hand side in (46) we write

$$\frac{\partial g_0}{\partial \tilde{\boldsymbol{\rho}}} = \boldsymbol{s}_f = \sum \boldsymbol{s}_{f,i}, \tag{47}$$

where $\boldsymbol{s}_f$ is a vector containing the derivatives of the objective function with respect to the filtered density field, $\sum$ is the assembly operator and $\boldsymbol{s}_{f,i}$ is the contribution to $\boldsymbol{s}_f$ of each element

$$\boldsymbol{s}_{f,i} = -q(1-\underline{p}) \left(\int_{\Omega_i^e} \boldsymbol{N}^e \tilde{\rho}_i^{q-1} \boldsymbol{u}^{eT} \boldsymbol{B}^{eT} \boldsymbol{D} \boldsymbol{B}^e \boldsymbol{u}^e \; dA \right), \tag{48}$$

since $P(\tilde{\rho}_i) = \underline{p} + (1-\underline{p})\tilde{\rho}_i^q$, and $\tilde{\rho}_i$ is the approximation of the filtered density field in element i, evaluated using Gauss quadrature with 4 Gauss points. The derivation of expression (48) can be found in Sigmund and Lazarov [14]. From equation (43), $\tilde{\boldsymbol{\rho}} = \hat{\boldsymbol{K}}^{-1} \boldsymbol{T} \boldsymbol{\rho}$, which implies that

$$\frac{\partial \tilde{\boldsymbol{\rho}}}{\partial \boldsymbol{\rho}} = \boldsymbol{T}^T \hat{\boldsymbol{K}}^{-1}. \tag{49}$$

Finally, insertion of (49) and (47) into (46) yields the sensitivity of g_0 with respect to the design variable $\boldsymbol{\rho}$ as

$$\frac{\partial g_0}{\partial \boldsymbol{\rho}} = \boldsymbol{T}^T \hat{\boldsymbol{K}}^{-1} \boldsymbol{s}_f. \tag{50}$$

Element based PDE-filter

The sensitivity of the objective function with respect to the design variable $\boldsymbol{\rho}$, can be written as

$$\frac{\partial g_0}{\partial \boldsymbol{\rho}} = \frac{\partial g_0}{\partial \hat{\boldsymbol{\rho}}} \frac{\partial \hat{\boldsymbol{\rho}}}{\partial \boldsymbol{\rho}}. \tag{51}$$

For the first term we can use expression (6) and expression (15) to conclude that

$$\begin{aligned} \frac{\partial g_0}{\partial \hat{\boldsymbol{\rho}}} &= \sum_{j=1}^{M_e} \frac{\partial g_0}{\partial \hat{\rho}_j} \boldsymbol{\delta_j} = \sum_{j=1}^{M_e} \left(\boldsymbol{u}_j^{eT} \frac{\partial P(\hat{\rho}_j)}{\partial \hat{\rho}_j} \boldsymbol{K_{0,j}^e} \boldsymbol{u}_j^e \right) \boldsymbol{e_j}^T \\ &= \sum_{j=1}^{M_e} \left(q(1-\underline{p}) \hat{\rho}_j^{q-1} \boldsymbol{u}_j^{eT} \boldsymbol{K_{0,j}^e} \boldsymbol{u}_j^e \right) \boldsymbol{e_j}^T, \end{aligned} \tag{52}$$

where $\boldsymbol{e_j}$ denotes a vector with length M_e with a 1 in the j:th coordinate and 0 elsewhere. By using the chain rule and combining (45) and (49) we have

$$\frac{\partial \hat{\boldsymbol{\rho}}}{\partial \boldsymbol{\rho}} = \boldsymbol{T^T} \hat{\boldsymbol{K}}^{\boldsymbol{-1}} \hat{\boldsymbol{T}}^{\boldsymbol{T}}. \tag{53}$$

Combining (53) and (52) provides the sensitivity of g_0 with respect to the design variable $\boldsymbol{\rho}$ as

$$\frac{\partial g_0}{\partial \boldsymbol{\rho}} = \frac{\partial g_0}{\partial \hat{\boldsymbol{\rho}}} \frac{\partial \hat{\boldsymbol{\rho}}}{\partial \boldsymbol{\rho}} = \boldsymbol{T^T} \hat{\boldsymbol{K}}^{\boldsymbol{-1}} \hat{\boldsymbol{T}}^{\boldsymbol{T}} \left(\sum_{j=1}^{M_e} \left(q(1-\underline{p}) \hat{\rho}_j^{q-1} \boldsymbol{u}_j^{eT} \boldsymbol{K_{0,j}^e} \boldsymbol{u}_j^e \right) \boldsymbol{e_j}^T \right). \tag{54}$$

6 Filtering using total variation

In this chapter, a TV-regularizing filter is presented. The goal of the filter is as with any other filter to avoid unwanted solutions, such as checker-boarding, but also to keep the total variation of the design variable at a controlled level.

6.1 TV-filter

By reformulating the potential functional (38) of the PDE-filter to

$$\Pi(\tilde{\rho}) = \int_\Omega l_0 |\nabla\tilde{\rho}|\ dA + \frac{1}{2}\int_\Omega |\rho - \tilde{\rho}|^2\ dA, \tag{55}$$

a PDE-filter with total variation regularization is created, where $|\nabla\tilde{\rho}|$ is approximated by the smooth approximation f_1, defined in expression (22),

$$\Pi(\tilde{\rho}) = \int_\Omega l_0 f_1(\nabla\rho) + \frac{1}{2}\int_\Omega |\rho - \tilde{\rho}|^2\ dA. \tag{56}$$

Minimization of the potential functional allows the filter equation to be expressed as

$$\begin{aligned} -l_0\nabla\cdot(f_1'(\nabla\tilde{\rho})) + \tilde{\rho} = \rho \text{ in } \Omega, \\ \boldsymbol{n}\cdot f_1'(\nabla\tilde{\rho}) = 0 \text{ on } \partial\Omega. \end{aligned} \tag{57}$$

Insertion of expression (35) into expression (57) yields

$$\begin{aligned} -l_0\nabla\cdot\left(\frac{\nabla\tilde{\rho}}{\sqrt{(\nabla\tilde{\rho})^2+\epsilon^2)}}\right) + \tilde{\rho} = \rho \text{ in } \Omega, \\ \boldsymbol{n}\cdot\left(\frac{\nabla\tilde{\rho}}{\sqrt{(\nabla\tilde{\rho})^2+\epsilon^2)}}\right) = 0 <=> \boldsymbol{n}\cdot\nabla\tilde{\rho} = 0 \text{ on } \partial\Omega. \end{aligned} \tag{58}$$

The same approach as for the nodal based PDE-filter is used to solve the filter equation for the TV-filter by the finite element method, where the discrete form of the TV-filter equation is

$$l_0\int_\Omega \boldsymbol{B^T D_\rho(\tilde{\rho}) B}\ dV\ \boldsymbol{\tilde{\rho}} + \int_\Omega \boldsymbol{N^T N}\ dV\ \boldsymbol{\tilde{\rho}} = \int_\Omega \boldsymbol{N^T}\ dV\ \boldsymbol{\rho}. \tag{59}$$

Analogously to the PDE-filter, we obtain a system on the form $\boldsymbol{K}_\rho\boldsymbol{\tilde{\rho}} = \boldsymbol{T\rho}$. The difference from the PDE-filter is that the filter operator $\boldsymbol{K_\rho} = \boldsymbol{K_\rho(D_\rho(\tilde{\rho}))}$ is dependent on the filtered density, resulting in the non-linear filter equation for the TV-filter

$$\boldsymbol{K_\rho(D_\rho(\tilde{\rho}))\tilde{\rho}} = \boldsymbol{T\rho}, \tag{60}$$

where the filter operator is calculated element-wise as

$$\boldsymbol{K^e_\rho(D^e_\rho)} = l_0\int_\Omega \boldsymbol{B^{eT} D^e_\rho(\tilde{\rho}) B^e}\ dV, \tag{61}$$

with

$$\boldsymbol{D}^{\boldsymbol{e}}_{\boldsymbol{\rho}}(\tilde{\boldsymbol{\rho}}^{e}) = \boldsymbol{I}\frac{1}{((\nabla\tilde{\boldsymbol{\rho}}^{e})^{T}\nabla\tilde{\boldsymbol{\rho}}^{\boldsymbol{e}} + \epsilon^{2})^{1/2}}, \tag{62}$$

and $\nabla\tilde{\boldsymbol{\rho}}^{\boldsymbol{e}}$ is a numerical approximation of $\nabla\tilde{\rho}$ evaluated in the center of the element. Since symmetric four node bi-linear elements are used

$$\nabla\tilde{\boldsymbol{\rho}}^{e} = \frac{1}{2h}\begin{bmatrix} -\tilde{\rho}^{e}_{1} + \tilde{\rho}^{e}_{2} + \tilde{\rho}^{e}_{3} - \tilde{\rho}^{e}_{4} \\ -\tilde{\rho}^{e}_{1} - \tilde{\rho}^{e}_{2} + \tilde{\rho}^{e}_{3} + \tilde{\rho}^{e}_{4} \end{bmatrix}, \tag{63}$$

where $\tilde{\boldsymbol{\rho}}^{\boldsymbol{e}}$ contains the filtered density node values, with local node indexing, for element e. Since $0 \leq \tilde{\rho}_i \leq 1$ it follows that $0 \leq \nabla\tilde{\boldsymbol{\rho}}^{\boldsymbol{e}} \leq \frac{1}{h}[1\ 1]^T$ and ϵ must be chosen such that $\epsilon << \frac{1}{h}$. Analogously with the element based PDE-filter, the element-wise constant filtered density vector is computed as

$$\hat{\boldsymbol{\rho}} = \hat{\boldsymbol{T}}(\boldsymbol{K}_{\boldsymbol{\rho}}(\boldsymbol{D}_{\boldsymbol{\rho}}(\tilde{\boldsymbol{\rho}})))^{-1}\boldsymbol{T}\boldsymbol{\rho}. \tag{64}$$

The non-linear filter equation (60) is solved using a modified version of Newton's method, described in box 2, where the approximation $\frac{\partial \boldsymbol{r}_{\boldsymbol{\rho}}}{\partial \tilde{\boldsymbol{\rho}}} = \boldsymbol{K}_{\boldsymbol{\rho}} + \frac{\partial \boldsymbol{K}_{\boldsymbol{\rho}}}{\partial \tilde{\boldsymbol{\rho}}}\tilde{\boldsymbol{\rho}} \approx \boldsymbol{K}_{\boldsymbol{\rho}}$ is used to avoid calculation of $\frac{\partial \boldsymbol{K}_{\boldsymbol{\rho}}}{\partial \tilde{\boldsymbol{\rho}}}$. The approximation causes the algorithm to converge slowly and is not recommended for a final implementation, but may be used for performing numerical experiments with a model mesh at low resolution.

```
Iterative solution algorithm:
- Calculate initial guess $\tilde{\boldsymbol{\rho}} = \boldsymbol{T}\boldsymbol{\rho}$
- Calculate $\boldsymbol{K}_{\boldsymbol{\rho}}(\tilde{\boldsymbol{\rho}})$
- Calculate residual $\boldsymbol{r}_{\boldsymbol{\rho}} = \boldsymbol{K}_{\boldsymbol{\rho}}(\tilde{\boldsymbol{\rho}})\tilde{\boldsymbol{\rho}} - \boldsymbol{T}\boldsymbol{\rho}$

• Loop while $||\boldsymbol{r}_{\boldsymbol{\rho}}||_2 > r_{tol}$ :
    - Calculate $\Delta\tilde{\boldsymbol{\rho}} = \boldsymbol{K}_{\boldsymbol{\rho}}^{-1}(-\boldsymbol{r}_{\boldsymbol{\rho}})$
    - Update $\tilde{\boldsymbol{\rho}} = \tilde{\boldsymbol{\rho}} + \Delta\tilde{\boldsymbol{\rho}}$
    - Calculate new $\boldsymbol{K}_{\boldsymbol{\rho}}(\tilde{\boldsymbol{\rho}})$
    - compute $\boldsymbol{r}_{\boldsymbol{\rho}} = \boldsymbol{K}_{\boldsymbol{\rho}}(\tilde{\boldsymbol{\rho}})\tilde{\boldsymbol{\rho}} - \boldsymbol{T}\boldsymbol{\rho}$
• end loop
```

Box 2: Pseudo code for the algorithm used to solve equation 60.

6.2 Implementation in topology optimziation

An unsuccessful attempt to use the TV-filter to control the perimeter for the optimization problem was done. It was found that the perimeter is not constant for a given length scale l_0, but dependent on the filtered variable $\tilde{\boldsymbol{\rho}}$. Due to time limitations, the relation between l_0 and the perimeter of the design was not further investigated.

7 Results

The results displayed are solutions to the "heat compliance" optimization problem with a mesh resolution of 256×256 elements unless otherwise specified. All derivatives that are calculated have been verified using the finite difference method, detailed in Appendix B, and all results are presented without post-processing.

7.1 Total variation constraint

The smooth approximation f_2 in (23) is used together with $\epsilon = 0.5$; a relatively large value of ϵ is needed to avoid oscillations in the design updates. The area fraction is limited to $\omega = 0.2$ and the upper bound on total variation, τ, is given in the tables below. The results are presented for both of the two penalization methods described in section 3.3. Due to oscillations in the design updates, the problem does not completely converge and the KKT-conditions, the standard convergence criteria in the MMA-solver, are not fulfilled. Therefore, the solution is accepted when a stagnation criteria is fulfilled, $||\boldsymbol{\rho}_n - \boldsymbol{\rho}_{n-1}||_2 < r_t$, where r_t is a tolerance and n the current iteration number. The designs shown in figure 9 are obtained with the modified SIMP-scheme in expression (10). The "combined penalization strategy", described in section 3.3, was used to achieve the results in figure 10. The development during the optimization of the designs C_1 and C_6 in figure 10 are shown in figure 11 and figure 12. Characteristics of the designs presented in figure 12 are tabulated in appendix A. Due to the inaccuracy of TV_4 as a measure of the perimeter when intermediate elements are included in the design, a more accurate measure of the perimeter, TV_4^{abs}, that is calculated using $\epsilon = 0$, is presented with the tabulated data and figures below.

Table 1: Characteristics for the designs in figure 9.

Figure	τ	Compliance	Area	TV_4	TV_4^{abs}	M_{nd}
S_1	1	189.8	0.2	1.000	6.745	0.2412
S_2	2	111.3	0.2	2.001	8,907	0.1871
S_3	4	78.4	0.2	4.001	12.013	0.1577
S_4	8	57.1	0.2	8.000	16.079	0.1255

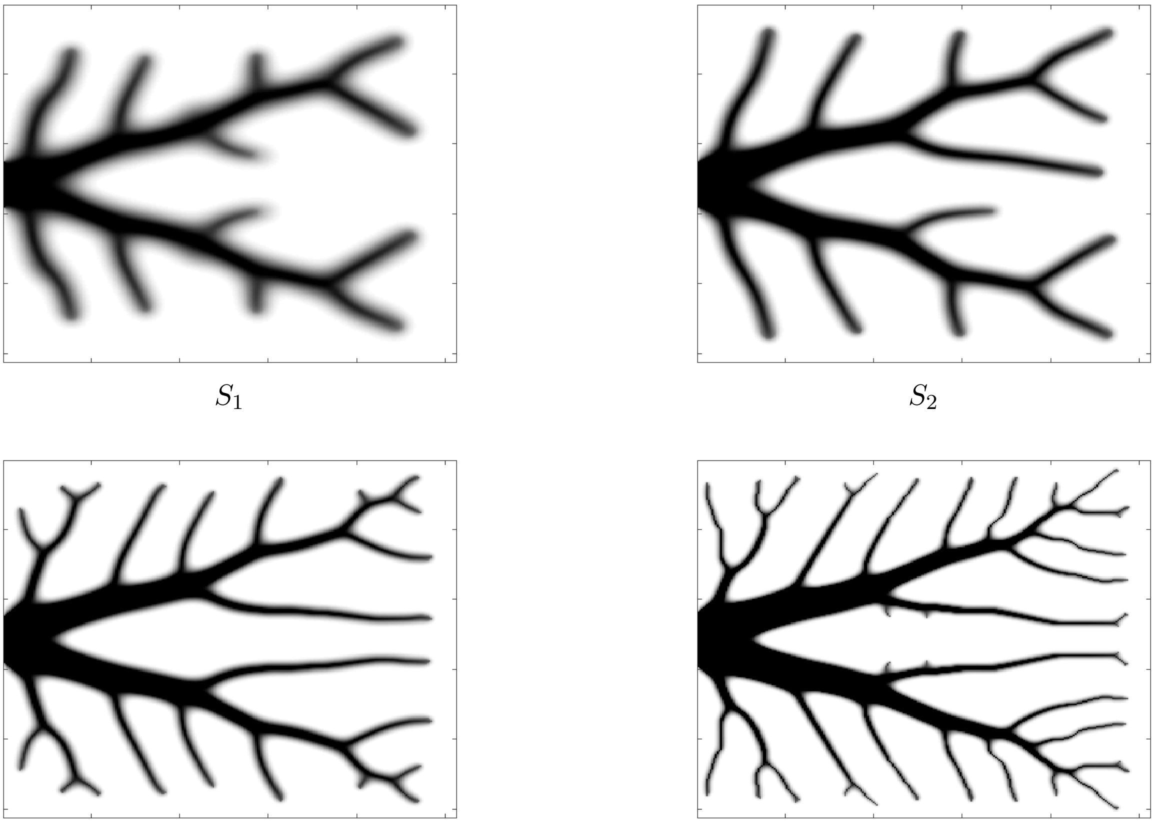

S_1 S_2

S_3 S_4

Figure 9: Solutions to the "heat compliance" optimization problem with a TV constraint, obtained with "modified SIMP" penalization.

Table 2: Characteristics for the designs in figure 10.

Figure	τ	Compliance	Area	TV_4	TV_4^{abs}	M_{nd}
C_1	3	339.5569	0.17529	4.2852	4.2852	4.6195e-08
C_2	4	298.2005	0.18452	4.5855	4.5862	7.2163e-06
C_3	5	215.5380	0.19386	5.6343	5.6354	1.0057e-05
C_4	6	172.0613	0.19327	6.6675	6.6675	4.5499e-08
C_5	7	154.3565	0.19264	7.1861	7.1861	4.5529e-08
C_6	8	142.3174	0.18988	7.9879	7.9879	4.5571e-08

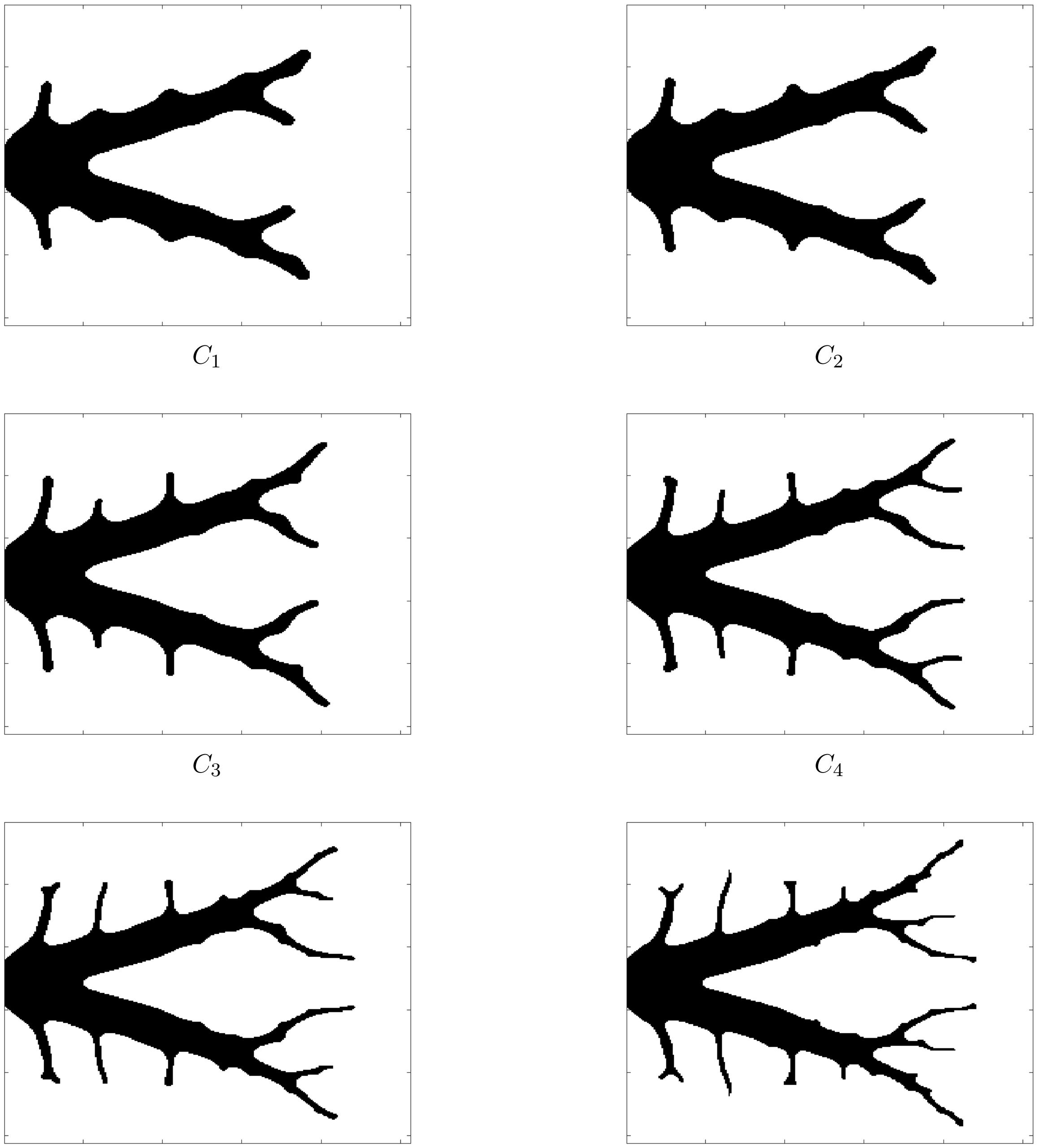

C_1 C_2

C_3 C_4

C_5 C_6

Figure 10: Solutions to the "heat compliance" optimization problem with a TV constraint, obtained with "combined penalization".

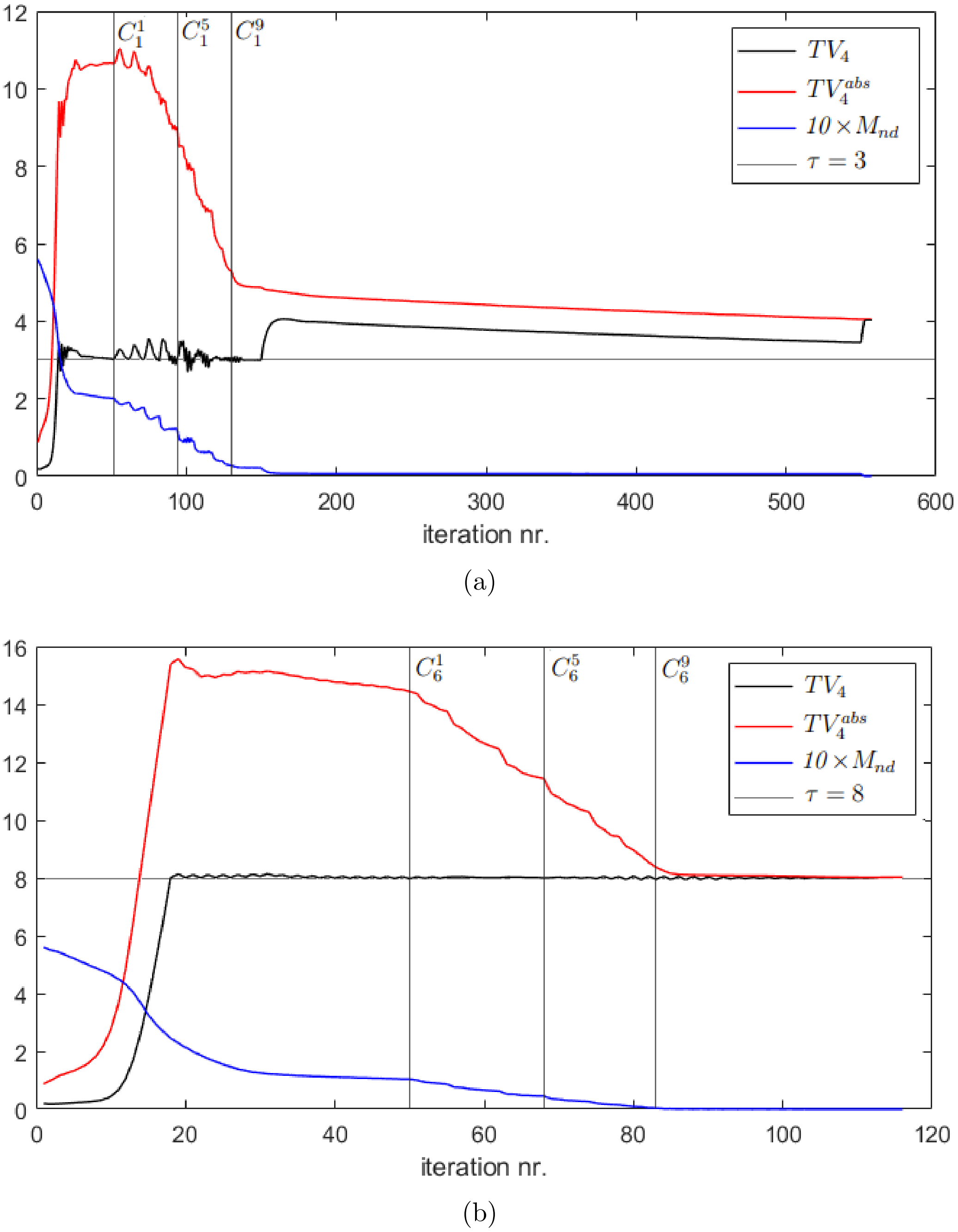

Figure 11: a) Evolution of C_1 with the designs for the penalization parameter $n = 1, 5, 9$ in (11) marked as C_1^1, C_1^5 and C_1^9 in the graph and are displayed in figure 12. b) Evolution of C_6 with the designs for the penalization parameter $n = 1, 5, 9$ in (11) marked as C_6^1, C_6^5 and C_6^9 in the graph and are displayed in figure 12.

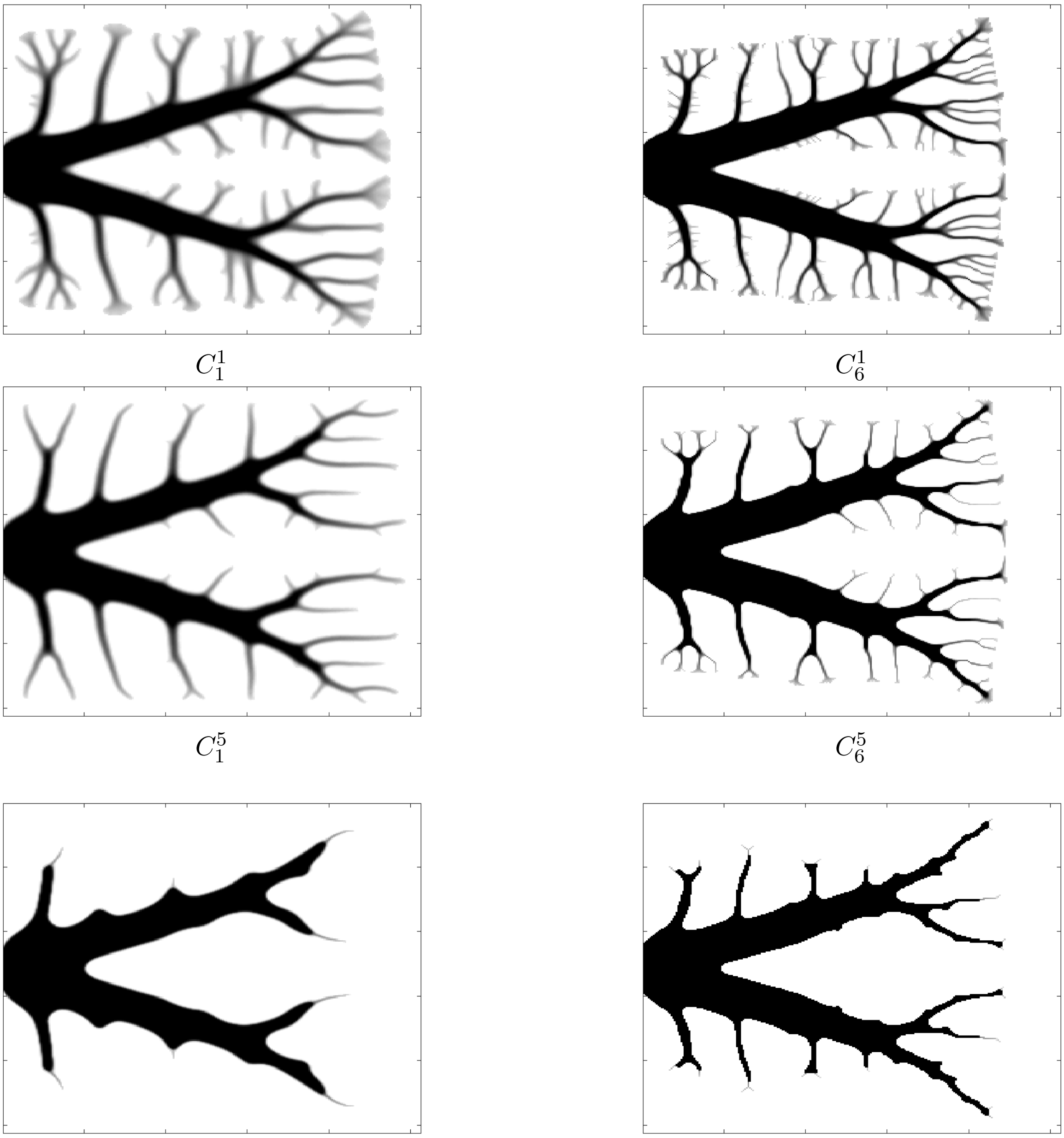

C_1^1 C_6^1

C_1^5 C_6^5

C_1^9 C_6^9

Figure 12: Design evolution for C_1 (left) and C_6 (right).

7.2 PDE-filter

The "modified SIMP-scheme" in expression (10) was used to obtain all numerical results in this section. The results $P_1 - P_2$, presented in figure 13, are included for comparing the nodal based PDE-filter with the element based PDE-filter and is solved with the volume constraint parameter $\omega = 0.5$. The computation time for the nodal based PDE-filter was approximately 14 times that of the element based PDE-filter. The results $P_3 - P_6$, presented in figure 14, was solved using the element based PDE-filter with the volume constraint parameter $\omega = 0.2$.

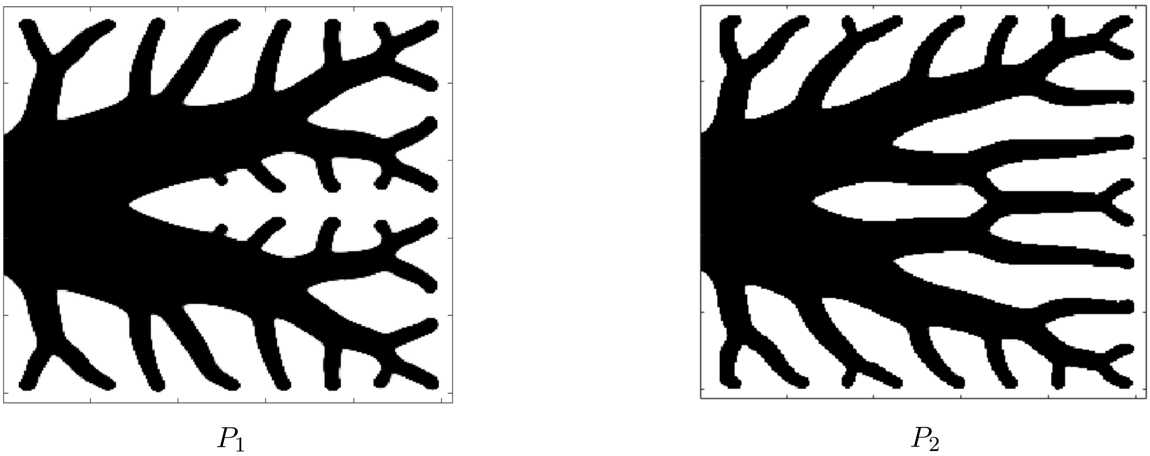
P_1

P_2

Figure 13: Comparison of numerical results obtained with the nodal based PDE-filter, P_1, and the element based PDE-filter, P_2.

Table 3: Characteristics for the designs in figure 13.

Figure	ω	l_0	Compliance	Area	M_{nd}
P_1	0.5	0.01m	21.44	0.5	0.0086
P_2	0.5	0.01m	20.33	0.5	0.0195

Table 4: Characteristics for the designs in figure 14.

Figure	ω	l_0	Compliance	Area	M_{nd}
P_3	0.2	0.01m	164.2	0.2	0.0003
P_4	0.2	0.005m	93.8	0.2	0.0001
P_5	0.2	0.0025m	66.7	0.2	0.0005
P_6	0.2	0.00125m	53.7	0.2	0.0011

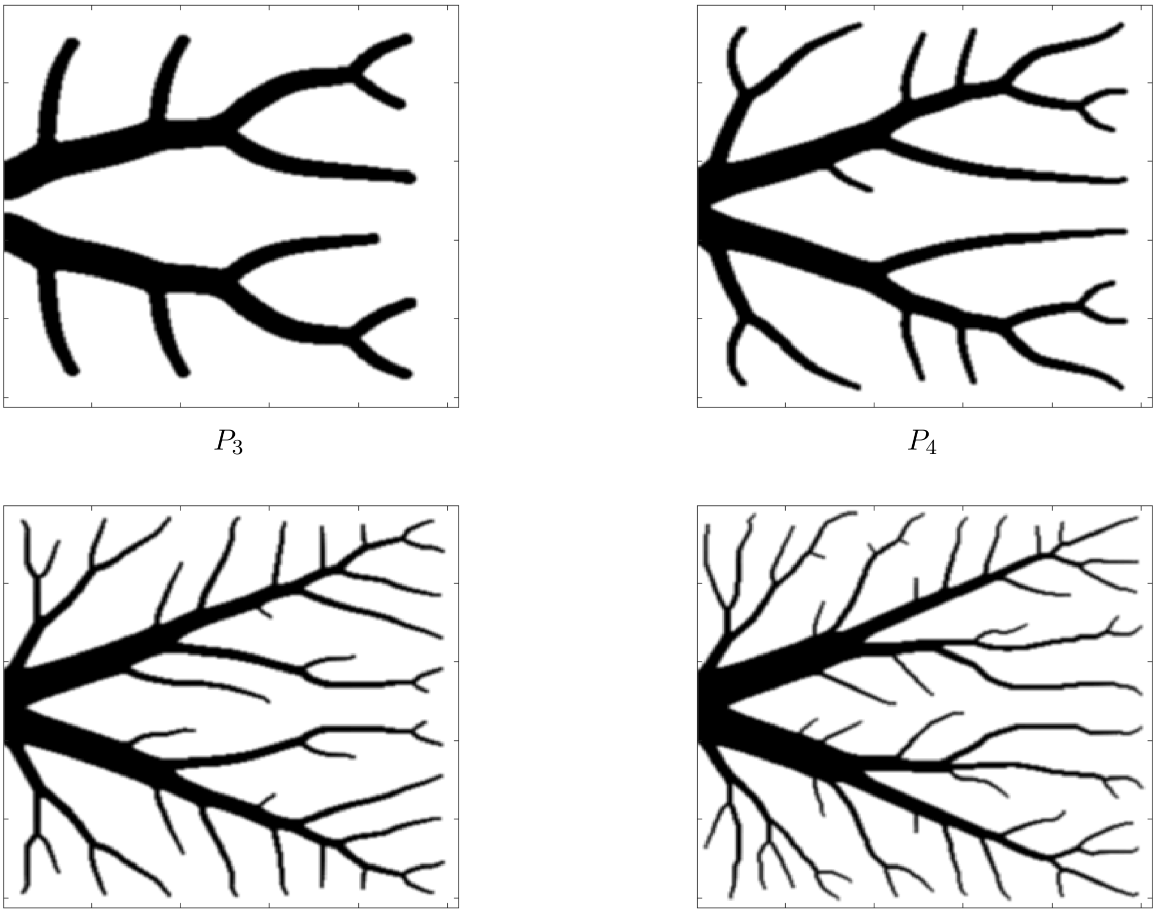

P_3 P_4

P_5 P_6

Figure 14: Designs obtained with the element based PDE-filter.

7.3 TV-filter

The TV-filter of section 6.1 is evaluated by filtering the binary "test image" in figure 15 with a resolution of 128×128 elements. The non-linear filter equation (60) is solved using the algorithm described in box 2, with the residual tolerance $r_{tol} = 10^{-4}$.

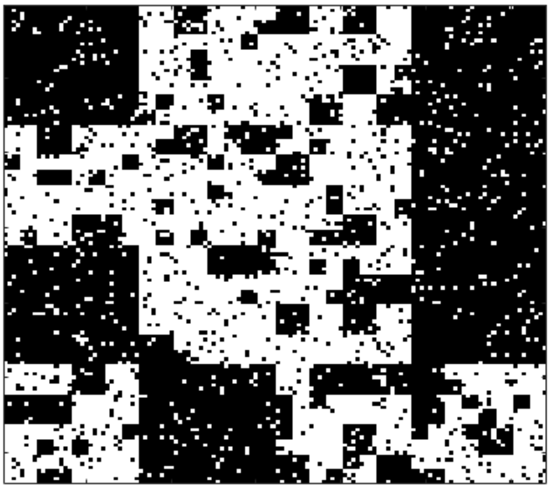

Figure 15: Binary image used to evaluate the TV-PDE-filter.

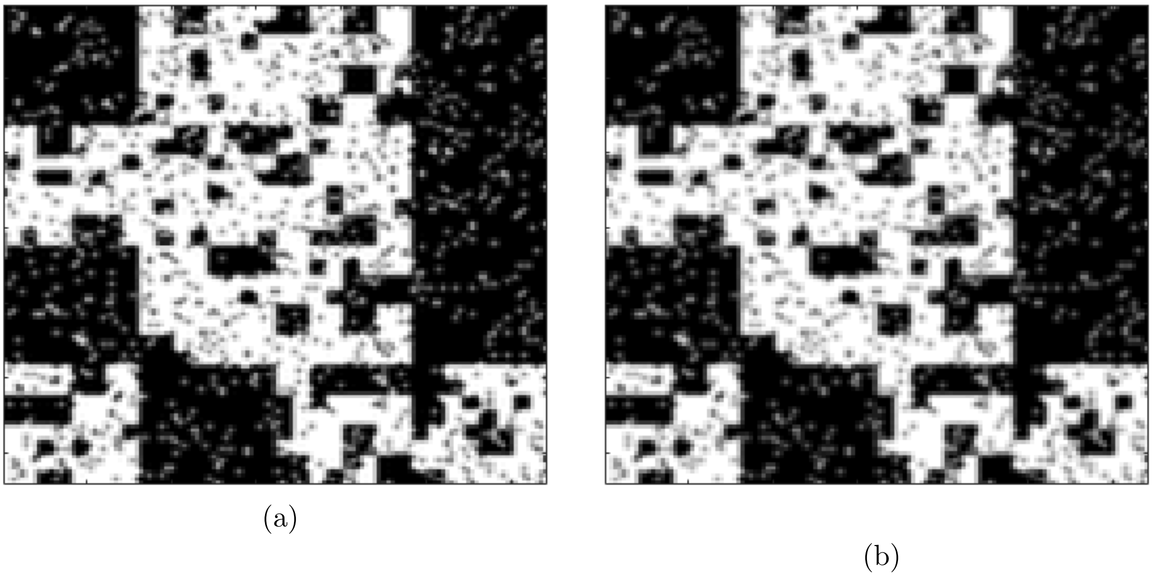

(a)

(b)

Figure 16: Binary test image filtered with the element based PDE-filter. a) $l_0 = 0.001$ b) $l_0 = 0.002$

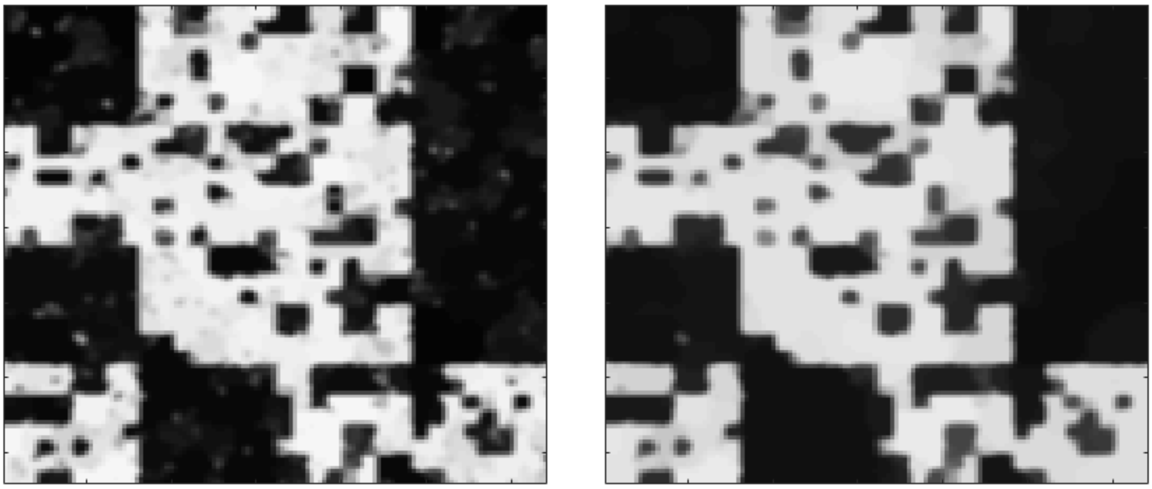

(a) (b)

Figure 17: Binary test image filtered with the TV-filter, $\epsilon = 10^{-4}$. a) $l_0 = 0.001$ b) $l_0 = 0.002$

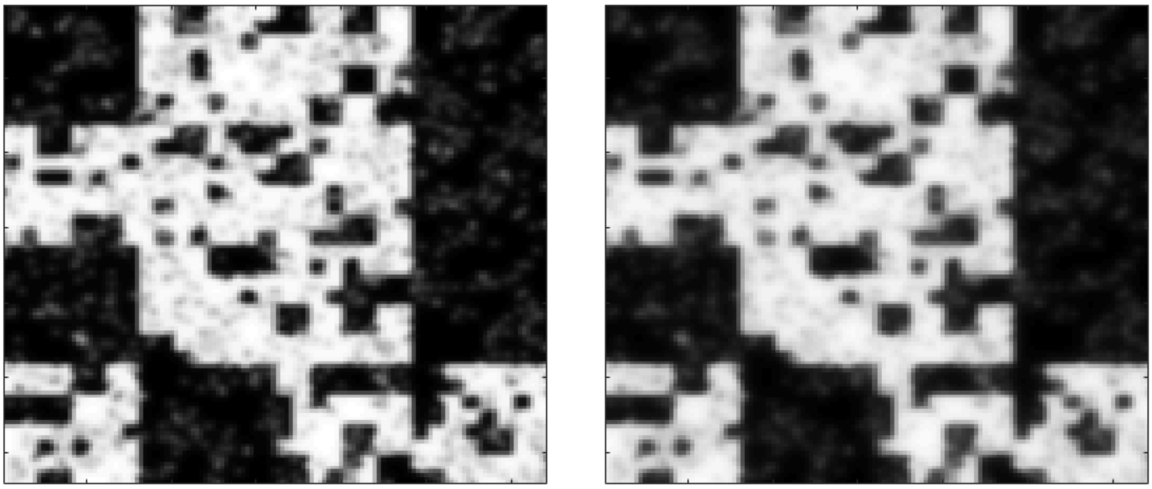

(a) (b)

Figure 18: Binary test image filtered with the TV-filter, $\epsilon = 10$. a) $l_0 = 0.001$ b) $l_0 = 0.002$

8 Discussion

8.1 Total variation constraint

It appears to be difficult to obtain a crisp black and white solution with the modified SIMP-scheme. The results S_1 to S_4, illustrated in figure 9, have blurred edges and the measure of non discreteness, M_{nd}, is relatively high, as seen in table 1. Since the total variation is underestimated for designs with blurred edges, as was discussed in section 4.2, the actual perimeters of the designs are significantly larger than the perimeter constraints, as seen in table 1 where TV_4^{abs} is a more accurate approximation of the perimeter than TV_4. This underestimation of the perimeter could be limited by choosing a smaller ϵ in the smooth approximation. However, the optimization problem is observed to be numerically unstable due to oscillations in the design updates when $\epsilon < b \approx 0.01$, detailed in section 8.1.1, and a discrete solution is difficult to obtain while $\epsilon > b \approx 0.01$.

The results C_1 to C_6, presented in figure 10, shows designs with various perimeters although the perimeter constraint is only fulfilled for C_6. In figure 12, it can be see that designs with blurred edges occurs early in the solution process that lowers the total variation TV_4. The estimated perimeter $TV_4 = 3.01$ compared to the more accurate measure $TV_4^{abs} = 10.56$ for C_1^1. For C_6^1 the estimated perimeter $TV_4 = 7.96$ while the more accurate estimation $TV_4^{abs} = 14.31$. It can be concluded that the constraint on TV_4 is fulfilled early in the solution process, while the perimeter is underestimated due to the smooth edges. As the penalization is increased, the underestimation of TV_4 decreases since the edges becomes crisper, leading to a more accurate estimation of the perimeter, as shown in figure 11. The cost for adding material in the void sections are increasing with increased penalization. As the penalisation parameter c_1 is increased, it eventually dominates the objective function causing elements where $\rho_i < 0.5$ to be forced to 0 by the optimization algorithm, while elements where $0.5 < \rho_i$ are forced to 1. This leads to the total variation constraint being violated since it is too costly to add material in the void areas to decrease the perimeter at this stage in the optimization process. This can be seen in figure 11 where the total variation constraint is violated in figure 11a after around 150 iterations while in 11b TV_4 converges to TV_4^{abs}.

The total variation constraint makes long thin arms costly due to their large circumference although there is no explicit penalty or constraint on the thickness of the arms. This allows for tapered arms to be formed, as can be seen in result C_6, illustrated in figure 10, which can be compared to result P_3, illustrated in figure 14, where the thickness of the arms are limited by the minimum radius $r = 2\sqrt{3}l_0$. For larger perimeter constraints τ, element-sized structures occurs in the solution. The design is then limited by the mesh and the refinement of the mesh allows for finer "arms" to be formed.

8.1.1 Blurring and numerical instabilities

The blurring of the edges of the designs can be explained by analysing the sensitivities of TV_4 with respect to $\boldsymbol{\rho}$. For simplicity, only the first term in expression (21), $TV_4^x(\boldsymbol{\rho})$, is considered. It can be seen from expression (31) that the sensitivity of TV_4^x with respect to one element density depends on the element itself and its two nearest neighbours, that is,

$$\frac{\partial TV_4^x}{\partial \tilde{\rho}_i} = C\left(f_n'(\Delta\rho_i) - f_n'(\Delta\rho_{i-1})\right) = C\left(\frac{\Delta\rho_i}{\sqrt{(\Delta\rho_i)^2+\epsilon^2}} - \frac{\Delta\rho_{i-1}}{\sqrt{(\Delta\rho_{i-1})^2+\epsilon^2}}\right), \tag{65}$$

where $\Delta\rho_i = \rho_i - \rho_{i+1}$ and C is a constant. If $\epsilon \to 0$, the derivative depends only on the "sign" of $\Delta\rho_i$ and $\Delta\rho_{i-1}$ and not on the magnitude,

$$\lim_{\epsilon\to 0} C\left(\frac{\Delta\rho_i}{\sqrt{(\Delta\rho_i)^2+\epsilon^2}} - \frac{\Delta\rho_{i-1}}{\sqrt{(\Delta\rho_{i-1})^2+\epsilon^2}}\right) = C(\operatorname{sgn}(\Delta\rho_i) - \operatorname{sgn}(\Delta\rho_{i-1})), \tag{66}$$

which holds for both approximation f_1 and f_2. If ρ_{i-1}, ρ_i and ρ_{i+1} are given such that $\Delta\rho_{i-1} >> \Delta\rho_i > 0$, as illustrated in figure 19a, and $\frac{\partial TV_4^x}{\partial \rho_i}$ is evaluated, equation (66) gives $f_n'(\Delta\rho_{i-1}) \approx f_n'(\Delta\rho_i) \to \frac{\partial TV_4}{\partial \rho_i} \approx 0$, if ϵ is chosen so small that $0 < \epsilon << \Delta\rho_i$. Note that $\frac{\partial TV_4}{\partial \rho_i} = 0$ if the absolute value function is used when calculating TV_4. If ϵ is instead chosen as a large number, e.g. $\epsilon = 0.1$, equation (65) yields, $f_n'(\Delta\rho_{i-1}) > f_n'(\Delta\rho_i) \to \frac{\partial TV_4}{\partial \rho_i} \approx -C$. Supposing that TV_4^x is minimized using a gradient based solution algorithm, ρ_i will be increased, leading to a smoother transition from ρ_{i-1} to ρ_{i+1}.

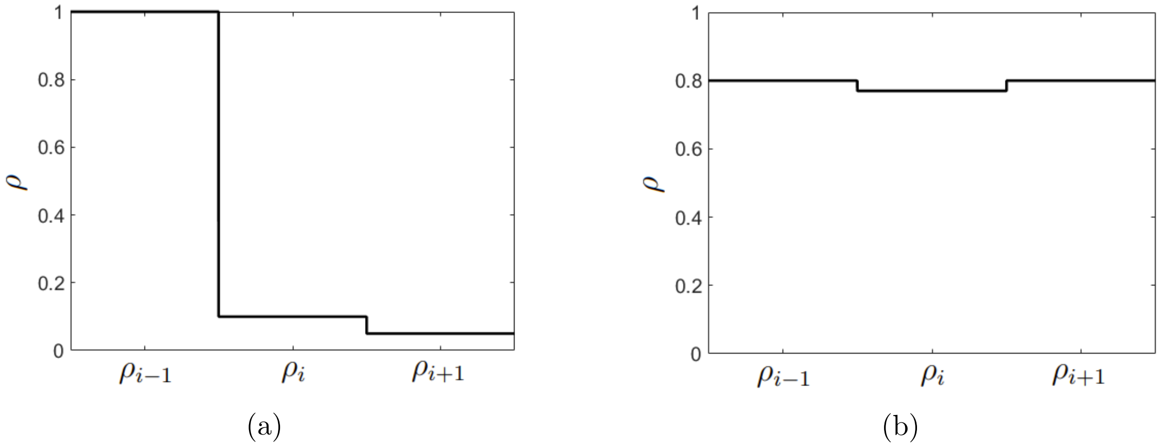

(a) (b)

Figure 19: Illustration of element densities.

To explain the numerical instabilities observed when $\epsilon < 0.01$, a case where $\Delta\rho_i = -\Delta\rho_{i+1}$, $0 < \Delta\rho_i << 1$, as in figure 19b, is considered. If $\epsilon << 1$, expression (66) shows that the derivative only depends on the signs of $\Delta\rho_i$ and $\Delta\rho_{i-1}$. More precisely, the derivative $\frac{\partial TV_4^x}{\partial \tilde{\rho}_i} = -C$ for all $\Delta\rho_i > 0$ and $\frac{\partial TV_4^x}{\partial \tilde{\rho}_i} = C$ for all $\Delta\rho < 0$. Thus $\frac{\partial TV_4^x}{\partial \tilde{\rho}_i} = 0$ only when $\Delta\rho$ is exactly 0. The solution does not converge unless $\rho_{i-1} = \rho_i = \rho_{i+1}$, which is not guaranteed since $\frac{\partial TV_4^x}{\partial \tilde{\rho}_i}$ does not approach 0 as $\rho_i \longrightarrow \rho_{i-1} = \rho_{i+1}$. Furthermore, as the density of the element ρ_i is increased in an update, the density of its neighbouring elements may be decreased, resulting in oscillations in the design updates.

8.2 PDE- and TV-filter

The element-based PDE-filter is significantly faster than the nodal-based PDE-filter while providing solutions with similar performance. With the nodal-based PDE-filter, l_0 has to be chosen with respect to the element side length h for the optimization problem to be numerically stable. The element-based PDE-filter was observed to be less sensitive to the relation between l_0 and h.

When comparing the filtered binary images in figures 16 to 18, the TV-filter seems to smear small structures in the image globally, rather than locally, as with the PDE-filter. It can also be seen that the TV-filter is edge-preserving, where the parameter l_0 seems to be related to a minimum dimension of any structure that is preserved, as seen by comparing figures 18b and figure 17b, where the element-sized structures are removed from the image, with figures 18a and 17a where element-sized structures can still be observed. The effect of ϵ is seen by comparing figure 17 and figure 18, where some local smearing of the structures can be seen in figure 18, where $\epsilon = 10$, that does not exist in figure 17, where $\epsilon = 10^{-4}$.

9 Conclusion and further work

The "TV constraint" method provides unsatisfying results due to the underestimation of the total variation as a result of the use of a smooth approximation of the absolute value function. A more exact approximation could be made, but increased complexity of the approximation increases computational costs. Also, the smooth approximations used in this thesis are convex functions that are easier to minimize than non-convex functions. Using a different solution method, or tweaking the MMA-solver in order to mitigate the numerical instabilities occurring when $\epsilon << 1$, could be investigated. Haber, et al. [9] report the need of fine tuning the solution parameters to achieve convergence, while Duysinx [19] successfully solves the optimization problem using the "dual method" with an internal loop procedure to approximate the perimeter constraint. The latter has not been investigated due to time limitations, and only minor experiments with adjusting the MMA-parameters have been performed.

Although the method does not allow exact control of the perimeter, some use in engineering may be found. With a carefully chosen penalization strategy and some tuning of the parameters in the solution algorithm, the method may provide useful results, where a trial and error approach could be used to find the sought perimeter.

The element based PDE-filter provides a more computationally efficient alternative to the nodal based PDE-filter, while no drawbacks has been observed. The TV-filter has not been successfully implemented to bound the perimeter of the designs in this thesis. Methods where the length scale parameter in (59) is updated at each iteration according to the current state, might be a way to control the perimeter of the design but has not been investigated due to time limitations.

An alternative approach to total variation regularization of a topology optimization problem, which has not been investigated in this thesis, is to use the proximal gradient method [20, 24] to solve the topology optimization problem. The proximal gradient method is designed for solving optimization problems on the form

$$\min_{\boldsymbol{x}} \{F(\boldsymbol{x}) = f(\boldsymbol{x}) + g(\boldsymbol{x})\}, \tag{67}$$

where $f(\boldsymbol{x})$ is differentiable and $g(\boldsymbol{x})$ is convex. The updates used to solve optimization problem (67) using the proximal gradient method are described in box 3.

Proximal gradient method:
- Initiate $\boldsymbol{x}^{\mathbf{0}}$
- for $k = 0, 1, ..., n$
• choose step size t_k
• update $\boldsymbol{x}^{k+1} = \text{prox}_{t_k g}(\boldsymbol{x}^k - t_k \nabla f(\boldsymbol{x}^k))$

Box 3: Proximal gradient method algorithm to solve the minimization problem (67).

The proximal operator $prox_g$, that appears in the update, is defined as

$$\operatorname{prox}_g(\boldsymbol{y}) = \arg\min_{\hat{\boldsymbol{y}}} g(\hat{\boldsymbol{y}}) + \frac{1}{2}||\hat{\boldsymbol{y}} - \boldsymbol{y}||_2^2. \tag{68}$$

Since the objective in the optimization problem (9) is differentiable and the total variation of a smooth density field (18) is a convex function [24], future investigations could apply the proximal gradient method to solve the optimization problem

$$\min_{\boldsymbol{\rho}} \; \boldsymbol{f^T u(\rho)} + \beta TV(\boldsymbol{\rho}). \tag{69}$$

References

[1] Kikuchi N Bendsøe M. "Generating optimal toplogies in structural design using a homogenization method". In: *Computer methods in applied mechanics and engineering* 71 (1988), pp. 197–224. DOI: `10.1016/0045-7825(88)90086-2`.

[2] Haber R B Chandrashekhar S J. "Stability of finite element models for distributed-parameter optimization and topology design". In: *Computational Methods in Applied Mechanics and Engineering* 130 (1996), pp. 203–226. DOI: `10.1016/0045-7825(95)00928-0`.

[3] Wallin M Ivarsson N Amir O Tortorelli D. "Consistent boundary conditions for PDE filter regularization in topology optimization". In: *Structural and Multidisciplinary Optimization* 62 (2020), pp. 1299–1311. DOI: `10.1007/s00158-020-02556-w`.

[4] Bruns TE Tortorelli DA. "Topology optimization of non-linear elastic structures and compliant mechanisms". In: *Comput. Methods Appl. Mech. Engrg.* 190 (1999), pp. 3443–3459.

[5] Sigmund O Diaz A. "Checkerboard patterns in layout optimization". In: *Structural Optimization* 10 (1995), pp. 40–45. DOI: `10.1007/BF01743693`.

[6] van Dijk NP Maute K Langelaar M van Keulen F. "Level-set methods for structural topology optimization: a review". In: *Struct Multidisc Optim* 48 (2013), pp. 437–472. DOI: `10.1007/s00158-013-0912-y`.

[7] Hägg L Wadbro E. "Nonlinear filters in topology optimization: existence of solutions and efficient implementation for minimum compliance problems". In: *Struct Multidisc Optim* 55 (2017), pp. 1017–1028. DOI: `10.1007/s00158-016-1553-8`.

[8] Hägg L Wadbro E. "On minimum length scale control in density based topology optimization". In: *Struct Multidisc Optim* 58 (2018), pp. 1015–1032. DOI: `10.1007/s00158-018-1944-0`.

[9] Jog C Haber R B Bendsøe M P. "A new approach to variable-topology shape design using a constraint on the perimeter". In: *Structural Optimization* 11 (1996), pp. 1–12.

[10] Bathe K J. *Finite Element Procedures.* Watertown, MA: Pretince Hall, 2006.

[11] Svanberg K. *MMA and GCMMA – two methods for nonlinear optimization.* Obtained from: `http://www.smoptit.se/` Accessed: 2021-04-28. KTH, Stockholm, Sweden, 2007.

[12] Svanberg K. *Svanberg matematisk optimering och IT AB, website.* `http://www.smoptit.se/`. Accessed: 2021-04-28.

[13] Svanberg K. "The method of moving asymptotes - a new method for structural optimization". In: *International journal for Numerical Methods in Engineering* 24 (1987), pp. 359–373. DOI: `10.1002/nme.1620240207`.

[14] Sigmund O Lazarov BS. "Filters in topology optimization based on Helmholtz-type differential equations". In: *International Journal for Numerical Methods in Engineering* 86 (2010), pp. 765–781.

[15] Beckers M. "Topology optimization using a dual method with discrete variables". In: *Structural Optimization* 17 (1999), pp. 14–24.

[16] Wallin M Ivarsson N Ristinmaa M. "Large strain phase-field multi-material topology optimization". In: *International Journal for Numerical Methods in Engineering* 104 (2015), pp. 887–904. DOI: `10.1002/nme.4962`.

[17] Sigmund O. "On the Design of Compliant Mechanisms Using Topology Optimization". In: *Journal of Structural Mechanics* 25(4) (1997), pp. 493–524. DOI: `10.1080/08905459708945415`.

[18] Petersson H Ottosen N. *Introduction to the Finite Element Method*. 1st ed. Prentice Hall, 1992.

[19] Duysinx P. "Layout optimization: A mathematical programming approach." In: *Structural Optimization* 16 (1998), pp. 68–75.

[20] Boyd S Parikh N. "Proximal Algorithms". In: *Foundations and Trends in Optimization* 1 (2013), pp. 123–231.

[21] Sigmund. "Morphology-based black and white filters for topology optimization". In: *Structural and Multidisciplinary Optimization* 33 (2007), pp. 401–424. DOI: `10.1007/s00158-006-0087-x`.

[22] Petersson J Sigmund O. "Numerical instabilities in topology optimization: A survey on procedures dealing with checkerboards, mesh-dependencies and local minima". In: *Structural Optimization* 16 (1998), pp. 68–75. DOI: `10.1007/BF01214002`.

[23] Borrwall T. "Topology optimization of elastic continua using restriction". In: *Archives of Computational Methods in Engineering* 8(4) (2001), pp. 351–385. DOI: `10.1007/BF02743737`.

[24] Chambolle A Caselles V Cremers D Novaga M Pock T. "An Introduction to Total Variation for Image Analysis". In: *Radon Series Comp. Appl. Math* 9 (2010), pp. 263–340.

Appendix A Data tables

Table 5: Characteristics for the designs in figure 12

Figure	c_1	Compliance	Area	TV_4	TV_4^{abs}	M_{nd}
C_1^1	0.001	61.2751	0.19988	3.0052	10.5599	0.1908
C_6^1	0.001	72.6355	0.19992	7.9599	14.3063	0.1009
C_1^5	0.025	68.1222	0.19312	2.9523	8.8820	0.1196
C_6^5	0.025	77.6393	0.19977	7.9400	11.0950	0.04043
C_1^9	0.589	207.4114	0.18142	3.0270	5.1865	0.02639
C_6^9	0.589	126.5289	0.19026	8.0466	8.1886	0.001428

Appendix B Accuracy of derivatives

To ensure that the correct derivatives are used in the optimization algorithm, the calculated values must be controlled in some way. This is done by comparing the computed analytical derivatives to numerically approximated derivatives. The numerical approximations are calculated using finite differences

$$\frac{\partial g_0}{\partial \rho_i} \approx \frac{g0(\boldsymbol{\rho} + h\boldsymbol{\delta_i}) - g0(\boldsymbol{\rho})}{h}, \tag{70}$$

where $\boldsymbol{\delta_i} = [\delta_{i,1}\ \delta_{i,2}\ ...\ \delta_{i,n}]^T$ and h is a step size. Expression (70) is only an accurate approximation around the point $g_o(\boldsymbol{\rho})$, thus if h is too large, the approximation is inaccurate. On the other hand, if h is chosen too small, the effects of round-off errors increase. There is in general no easy way to determine the correct step size h. A trial and error approach is used, where, if a reasonable h is found where the derivatives coincide with the analytical values for a number of randomly chosen indices i, the derivatives are assumed to be correctly calculated. Analogously, if no h is found where the numerical and analytical values agree, the analytical derivatives are assumed to be miscalculated values.

Appendix C Finite Element Formulation

The finite element formulation is presented for the solution of the heat equation in a 2-dimensional setting. The results are used directly for solving the heat flow problem in the "heat compliance" optimization problem but also to solve the PDE-filter and the TV-filter equations. For a more thorough explanation the reader can consult chapters 4, 6 and 10 in *Introduction to the Finite Element Method* [18].

C.1 Heat equation formulation for two-dimensional heat flow

Fourier's law for two-dimensional heat flow in a body with homogeneous material reads

$$\boldsymbol{q} = -\boldsymbol{D}\nabla T. \tag{71}$$

Where $\boldsymbol{q} = [q_x \; q_y]^T$ is the heat flux vector [W/m^2],$\nabla T = [\frac{\partial T}{\partial x} \frac{\partial T}{\partial y}]^T$ is the temperature gradient and $\boldsymbol{D} = \begin{bmatrix} k_{xx} & k_{xy} \\ k_{yx} & k_{yy} \end{bmatrix}$ is the constitutive matrix containing the directional heat transfer properties of the material. Matrix $\boldsymbol{D}$ is symmetric and positive definite. $\boldsymbol{D}$ is constant within a body with homogeneous material, and for a homogeneous isotropic material $\boldsymbol{D} = \alpha \boldsymbol{I}$, where $\alpha > 0$ is constant.

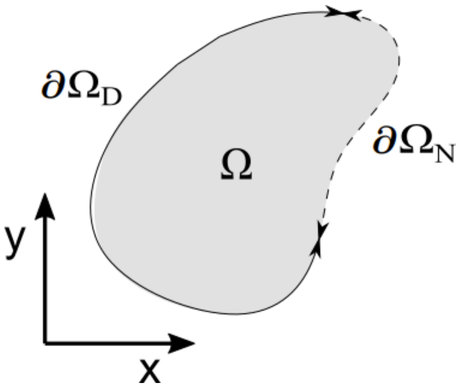

Figure 20: Illustration of an arbitrary 2-dimensional region Ω with boundary $\partial\Omega = \partial\Omega_N \cup \partial\Omega_D$.

We consider a 2-dimensional region Ω as in figure 20, occupied with a homogeneous material with boundary $\partial\Omega = \partial\Omega_D \cup \partial\Omega_N$ and being in thermal equilibrium. If we let Q be the amount of heat supplied to the body per area unit and time $[W/m^2]$, we may establish an energy balance equation given that the amount of added heat, per time unit, must equal the net flux of heat through the boundary in any part of Ω. The energy balance equation for $V \subset \Omega$ reads

$$\int_V Q \, dA = \oint_{\partial V} \boldsymbol{q^T n} \, dL, \tag{72}$$

where $\boldsymbol{n}$ is the outward-directed normal vector at the boundary and V is an arbitrary region that belongs to Ω. Applying Gauss divergence theorem to equation (72) gives

$$\int_V Q\ dA = \int_V \nabla \cdot (\boldsymbol{q})\ dA \Rightarrow \int_V [Q - \nabla \cdot \boldsymbol{q}]\ dA = 0 \tag{73}$$

and since V is arbitrary we may conclude that

$$\nabla \cdot\ (\boldsymbol{q}) = Q \tag{74}$$

which together with (71) gives us

$$\nabla \cdot (\boldsymbol{D} \nabla T) + Q = 0\ , \quad in\ \Omega\ . \tag{75}$$

Boundary conditions are needed to solve equation (75) and may be on the form

$$\begin{cases} \boldsymbol{n \cdot D} \nabla T = h_N, & on\ \partial\Omega_N \\ \qquad\quad T\ = t_D, & on\ \partial\Omega_D \end{cases} \tag{76}$$

for the region in figure 20, if the temperature T is known on $\partial\Omega_D$.

C.2 Variational (weak) form of heat flow in a two-dimensional body

To solve equation (75) using the finite element method, we rewrite the equation on the variational (weak) form. By multiplying with the arbitary function $v(x, y)$, that vanishes on $\partial\Omega_D$, and integrating over the domain Ω we get

$$\int_\Omega v\ \nabla \cdot \boldsymbol{q}\ dA - \int_\Omega vQ\ dA = 0. \tag{77}$$

Applying Green-Gauss theorem to the first term in (77) and using integration by parts yields

$$\int_\Omega (\nabla v)^T \boldsymbol{q}\ dA = \oint_{\partial\Omega} v \boldsymbol{q^T n}\ dL - \int_\Omega vQ\ dA. \tag{78}$$

Insertion into expression (77) gives

$$\int_\Omega (\nabla v)^T \boldsymbol{D} \nabla T\ dA = -\oint_{\partial\Omega} v \boldsymbol{q^T n}\ dL + \int_\Omega vQ\ dA. \tag{79}$$

Which is the variational form of heat flow in a two-dimensional body. If we use the typical boundary conditions specified in expression (76) and insert $q_n = \boldsymbol{q^T n}$, we have

$$\begin{aligned} \int_\Omega (\nabla v)^T \boldsymbol{D} \nabla T\ dA &= -\oint_{\partial\Omega_N} v h_N\ dL - \oint_{\partial\Omega_D} v q_n\ dL + \int_\Omega vQ\ dA \\ &= -\oint_{\partial\Omega_N} v h_N\ dL + \int_\Omega vQ\ dA \\ &\quad with\ T = t_D\ on\ \partial\Omega_D\ , \end{aligned} \tag{80}$$

since $v = 0$ on $\partial\Omega_D$.

C.3 Discretization

The region is discretized into a Cartesian mesh with $M_e = M_x \times M_y$ number of elements each having n number of nodes resulting in a total M_n number of nodes. The number of degrees of freedom equals the number of nodes for the heat flow problem. The temperature field in the body is interpolated using the element shape functions

$$T = \boldsymbol{N}\boldsymbol{u} \tag{81}$$

where $\boldsymbol{u} = [u_1 u_2 ... u_{M_n}]^T$ is the node temperature vector containing the unknown node temperatures, $\boldsymbol{N} = [\boldsymbol{N}_1 \boldsymbol{N}_2 ... \boldsymbol{N}_{M_n}]$ is the global shape function matrix containing the element shape function vectors $\boldsymbol{N_i} = [N_1^e N_2^e ... N_n^e]^T$, where $N_1^e N_2^e ... N_n^e$ are the element shape functions. The element shape functions are functions of the global coordinates (x,y) with the properties that $\boldsymbol{N_i^e} = 1$, in node i and 0 in all other nodes of the element. ∇T is described as

$$\nabla T = \nabla(\boldsymbol{N}\boldsymbol{u}) = \boldsymbol{B}\boldsymbol{u} \tag{82}$$

where $\boldsymbol{B} = \nabla \boldsymbol{N}$. Insertion into (80) yields

$$\left(\int_\Omega (\nabla v)^T \boldsymbol{D}\boldsymbol{B} \; dA\right) \boldsymbol{u} = -\oint_{\partial\Omega_N} v h_N \; dL + \int_\Omega vQ \; dA \tag{83}$$

and since v is arbitrary we may choose v freely. The Galerkin method is used where $v = \boldsymbol{N}\boldsymbol{c} \Rightarrow \nabla \boldsymbol{v} = \boldsymbol{B}\boldsymbol{c}$ is chosen where $\boldsymbol{c}$ is arbitrary and $\boldsymbol{N}\boldsymbol{c} = \boldsymbol{c^T}\boldsymbol{N^T}$ holds. Insertion into (83) gives

$$\left(\int_\Omega \boldsymbol{c^T}\boldsymbol{B^T}\boldsymbol{D}\boldsymbol{B} \; dA\right) \boldsymbol{u} = -\oint_{\partial\Omega_N} \boldsymbol{c^T}\boldsymbol{N^T} h_N \; dL + \int_\Omega \boldsymbol{c^T}\boldsymbol{N^T} Q \; dA. \tag{84}$$

Since $\boldsymbol{c}$ is arbitrary

$$\left(\int_\Omega \boldsymbol{B^T}\boldsymbol{D}\boldsymbol{B} \; dA\right) \boldsymbol{u} = -\oint_{\partial\Omega_N} \boldsymbol{N^T} h_N \; dL + \int_\Omega \boldsymbol{N^T} Q \; dA, \tag{85}$$

which is the discrete form of the variational formulation of the 2-dimensional heat flow problem.

C.4 Finite element equation

Equation (85) can be written as

$$\boldsymbol{K}\boldsymbol{u} = \boldsymbol{f_b} + \boldsymbol{f_l} \tag{86}$$

with $\boldsymbol{K} = \int_\Omega \boldsymbol{B^T} \boldsymbol{D} \boldsymbol{B} \; dA$ is the stiffness matrix, $\boldsymbol{f_b} = -\oint_{\partial\Omega_N} \boldsymbol{N^T} h_N \; dL$ is the boundary vector and $\boldsymbol{f_l} = \int_\Omega \boldsymbol{N^T} \boldsymbol{Q} \; dA$ is the load vector. We may also combine the boundary vector and the load vector to rewrite equation (86) on the more compact form

$$\boldsymbol{K}\boldsymbol{u} = \boldsymbol{f}, \tag{87}$$

which is a linear system of equations that may be solved using the boundary conditions given in expression (76).

C.5 Four node bilinear elements

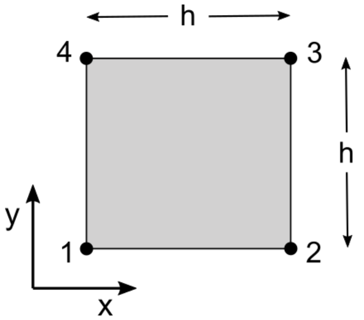

Figure 21: 4-node square element with side length h.

For a four node bilinear element with node coordinates $[(x_1, y_1); (x_2, y_2); (x_3, y_3); (x_4, y_4)]$, the element shape functions are

$$\begin{aligned} N_1^e(x,y) &= \frac{x - x_2}{x_1 - x_2} \frac{y - y_4}{y_1 - y_4}, \\ N_2^e(x,y) &= \frac{x - x_1}{x_2 - x_1} \frac{y - y_3}{y_2 - y_3}, \\ N_3^e(x,y) &= \frac{x - x_4}{x_3 - x_4} \frac{y - y_2}{y_3 - y_2}, \\ N_4^e(x,y) &= \frac{x - x_3}{x_4 - x_3} \frac{y - y_1}{y_4 - y_1}. \end{aligned} \tag{88}$$

If the elements are squares, with the edges parallel to the coordinate axes, as in figure 21, the element shape functions are simplified since $x_1 = x_4$, $x_2 = x_3$, $y_1 = y_2$ and $y_3 = y_4$ which gives $x_1 - x_2 = x_4 - x_3 = h$ and $y_1 - y_4 = y_2 - y_3 = h$, where h is the element side length. The element shape functions for a square element, illustrated in figure 22a, are

$$
\begin{aligned}
N_1^e(x,y) &= \frac{1}{h^2}(x-x_2)(y-y_4),\\
N_2^e(x,y) &= \frac{-1}{h^2}(x-x_1)(y-y_3),\\
N_3^e(x,y) &= \frac{1}{h^2}(x-x_4)(y-y_2),\\
N_4^e(x,y) &= \frac{-1}{h^2}(x-x_3)(y-y_1).
\end{aligned} \tag{89}
$$

For one element the B-matrix can be computed as

$$
\boldsymbol{B^e} = \nabla \boldsymbol{N^e} = \begin{bmatrix} \frac{\partial \boldsymbol{N}^e}{\partial x} \\ \frac{\partial \boldsymbol{N}^e}{\partial y} \end{bmatrix} = \begin{bmatrix} \frac{\partial N_1^e}{\partial x} & \frac{\partial N_2^e}{\partial x} & \cdots & \frac{\partial N_n^e}{\partial x} \\ \frac{\partial N_1^e}{\partial y} & \frac{\partial N_2^e}{\partial y} & \cdots & \frac{\partial N_n^e}{\partial y} \end{bmatrix}. \tag{90}
$$

Computation of $\nabla \boldsymbol{N^e}$ from expression (88) or (89) is straightforward and therefore left to the reader.

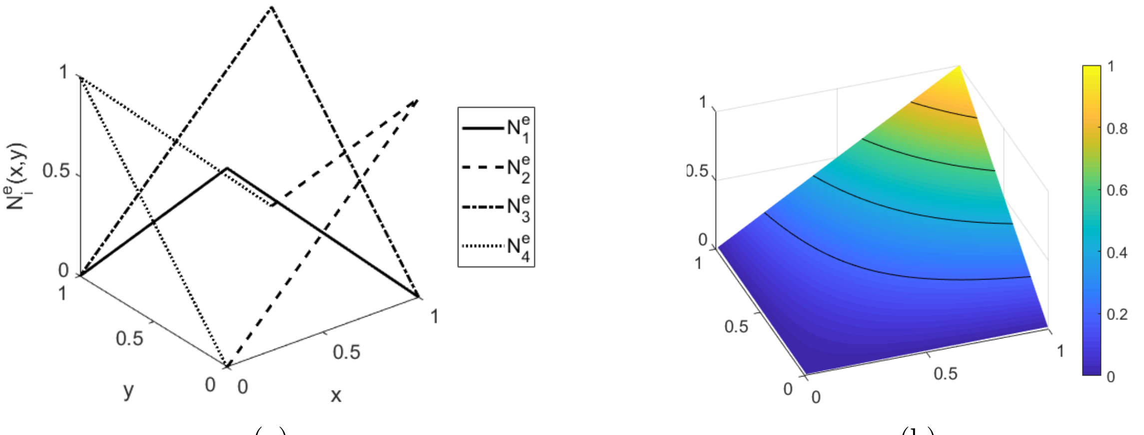

(a) (b)

Figure 22: a) Element shape functions for an element with side length $h = 1$. b) Temperature distribution with node temperature 1 at node 3, and 0 at the other three nodes.